Neurobiology of Disease

Loss of Activity-Induced Mitochondrial ATP Production Underlies the Synaptic Defects in a *Drosophila* Model of ALS

Nicholas E. Karagas,[1,5] Richa Gupta,[1] Elham Rastegari,[1] Kai Li Tan,[2,3,4] Ho Hang Leung,[7] Hugo J. Bellen,[2,3,4] Kartik Venkatachalam,[1,5,6] and Ching-On Wong[7]

[1]Department of Integrative Biology and Pharmacology, McGovern Medical School at the University of Texas Health Sciences Center, Houston, Texas 77030, [2]Departments of Molecular and Human Genetics and Neuroscience, Baylor College of Medicine, Houston, TX 77030, [3]Graduate Program in Developmental Biology, Baylor College of Medicine, Houston, Texas 77030, [4]Duncan Neurological Research Institute, Texas Children Hospital, Houston, Texas 77030, [5]Graduate Program in Biochemistry and Cell Biology, MD Anderson Cancer Center and University of Texas Health Sciences Center Graduate School of Biomedical Sciences, Houston, TX, 77030, [6]Graduate Program in Neuroscience, MD Anderson Cancer Center and University of Texas Health Sciences Center Graduate School of Biomedical Sciences, Houston, TX, 77030, and [7]Department of Biological Sciences, Rutgers University, Newark, New Jersey 07102

Mutations in the gene encoding vesicle-associated membrane protein B (VAPB) cause a familial form of amyotrophic lateral sclerosis (ALS). Expression of an ALS-related variant of *vapb* (*vapb*^{P58S}) in *Drosophila* motor neurons results in morphologic changes at the larval neuromuscular junction (NMJ) characterized by the appearance of fewer, but larger, presynaptic boutons. Although diminished microtubule stability is known to underlie these morphologic changes, a mechanism for the loss of presynaptic microtubules has been lacking. By studying flies of both sexes, we demonstrate the suppression of *vapb*^{P58S}-induced changes in NMJ morphology by either a loss of endoplasmic reticulum (ER) Ca^{2+} release channels or the inhibition Ca^{2+}/calmodulin (CaM)-activated kinase II (CaMKII). These data suggest that decreased stability of presynaptic microtubules at *vapb*^{P58S} NMJs results from hyperactivation of CaMKII because of elevated cytosolic [Ca^{2+}]. We attribute the Ca^{2+} dyshomeostasis to delayed extrusion of cytosolic Ca^{2+}. Suggesting that this defect in Ca^{2+} extrusion arose from an insufficient response to the bioenergetic demand of neural activity, depolarization-induced mitochondrial ATP production was diminished in *vapb*^{P58S} neurons. These findings point to bioenergetic dysfunction as a potential cause for the synaptic defects in *vapb*^{P58S}-expressing motor neurons.

Key words: **ALS; *Drosophila* neurobiology; ER calcium channels; mitochondrial ATP production; neurodegeneration; VAPB**

Significance Statement

Whether the synchrony between the rates of ATP production and demand is lost in degenerating neurons remains poorly understood. We report that expression of a gene equivalent to an amyotrophic lateral sclerosis (ALS)-causing variant of vesicle-associated membrane protein B (VAPB) in fly neurons decouples mitochondrial ATP production from neuronal activity. Consequently, levels of ATP in mutant neurons are unable to keep up with the bioenergetic burden of neuronal activity. Reduced rate of Ca^{2+} extrusion, which could result from insufficient energy to power Ca^{2+} ATPases, results in the accumulation of residual Ca^{2+} in mutant neurons and leads to alterations in synaptic vesicle (SV) release and synapse development. These findings suggest that synaptic defects in a model of ALS arise from the loss of activity-induced ATP production.

Received Dec. 14, 2021; revised Aug. 23, 2022; accepted Aug. 27, 2022.

Author contributions: N.E.K., K.L.T., H.J.B., K.V., and C.-O.W. designed research; N.E.K., R.G., E.R., K.L.T., H.H.L., K.V., and C.-O.W. performed research; N.E.K., K.L.T., K.V., and C.-O.W. analyzed data; N.E.K., K.L.T., H.J.B., K.V., and C.-O.W. edited the paper; K.V. wrote the first draft of the paper; K.V. and C.-O.W. wrote the paper.

This work was supported by the National Institutes of Health Grants R03AG063251 (to C.-O.W.), RF1AG069076 (to K.V.), RF1AG067414 (to K.V.), and R21AG072176 (to K.V.). We thank the Bloomington *Drosophila* Stock Center for fly stocks. We also thank Yufang Chao for technical help. Confocal and live cell microscopy were performed at the University of Texas Health Sciences Center Center for Advanced Microscopy, Department of Integrative Biology and Pharmacology at McGovern Medical School, and the Advanced Imaging Core, Department of Biological Sciences, Rutgers University, Newark.

N. E. Karagas' present address: Department of Neurology, University of Washington, Seattle, Washington 98195.

K. L. Tan's present address: Emergent BioSolutions, Gaithersburg, Maryland 20879.

R.G. and E.R. contributed equally to this work.

The authors declare no competing financial interests.

Correspondence should be addressed to Kartik Venkatachalam at kartik.venkatachalam@uth.tmc.edu or Ching-On Wong at chingon.wong@rutgers.edu.

https://doi.org/10.1523/JNEUROSCI.2456-21.2022

Copyright © 2022 the authors

Introduction

Amyotrophic lateral sclerosis (ALS) is an untreatable neurodegenerative disease characterized by the progressive loss of motor function leading to paralysis and death by respiratory failure (Taylor et al., 2016). Mutations in many genes have been implicated in the onset of the familial forms of the disease, which result in one or more of the following, disrupted nucleocytoplasmic transport, proteostatic imbalance, alterations in RNA metabolism, genome instability, mitochondrial dysfunction, aberrant Ca^{2+} homeostasis, neuronal hyperexcitability, and neuroinflammation (Ling et al., 2013; Selfridge et al., 2013; Taylor et al., 2016; Lin et al., 2017; Frere and Slutsky, 2018). In this study, we sought to examine the mechanisms of neuronal dysfunction in flies expressing a missense variant of *vapb*, which is equivalent to the human variant that causes a familial form of ALS (ALS8) in humans (Nishimura et al., 2004, 2005; Kanekura et al., 2006; Marques et al., 2006; Landers et al., 2008). We chose vesicle-associated membrane protein B (VAPB) because of the importance of this protein to neuronal viability. In addition to the missense variant that functions via a dominant-negative mechanism (Ratnaparkhi et al., 2008), spinal cords from patients with sporadic cases of ALS exhibit decreased *VAPB* expression (Anagnostou et al., 2010; Mitne-Neto et al., 2011). Defective VAPB function is also observed in Parkinson's disease (Kun-Rodrigues et al., 2015; Paillusson et al., 2017; Boczonadi et al., 2018).

At the molecular level, VAPB is a single-pass endoplasmic reticulum (ER) membrane protein that has been proposed to regulate mTOR signaling, autophagy, lysosomal acidification, proteasomal degradation/ER quality control, and formation of interorganellar contacts that link the ER to endosomes, peroxisomes, Golgi, and mitochondria (Peretti et al., 2008; De Vos et al., 2012; Deivasigamani et al., 2014; Moustaqim-Barrette et al., 2014; Roulin et al., 2014; Dong et al., 2016; Stoica et al., 2016; Hua et al., 2017; Zhao et al., 2018; Chaplot et al., 2019; Mao et al., 2019; Şentürk et al., 2019). Via its role in the formation of ER–mitochondria contacts, VAPB orchestrates the transfer of Ca^{2+} from ER into the mitochondrial matrix, and thereby, regulates ATP synthesis (De Vos et al., 2012; Stoica et al., 2016; Gomez-Suaga et al., 2017; Smith et al., 2017; Xu et al., 2020; Wong et al., 2021).

Expression of the ALS-related variants of *vapb* in *Drosophila* neurons has been shown to result in morphologic alterations in both axons and dendrites (Chai et al., 2008; Ratnaparkhi et al., 2008; Kamemura et al., 2021). Although it is known that defects in the development of the axon termini stem from diminished stability of presynaptic microtubules (Chai et al., 2008; Ratnaparkhi et al., 2008), exactly how mutant VAPB disrupts the microtubule cytoskeleton has remained unknown. In order to uncover the underlying molecular mechanism, we sought to examine genetic interactions between the *vapb* variant and genes encoding ER Ca^{2+} channels whose absence elicits phenotypes that ostensibly resemble those evoked by mutant *vapb* (Wong et al., 2014). These studies revealed that the phenotypes arising from the expression of mutant *vapb* are a consequence of presynaptic Ca^{2+} dyshomeostasis, which could stem from the inability of the neurons to synthesize the ATP molecules needed for Ca^{2+} extrusion. Our findings agree with the insights gleaned from *in silico* modeling of ALS neurons (Le Masson et al., 2014), and provide a possible explanation for the presynaptic defects associated with the expression of the ALS-causing variant of *vapb* in *Drosophila* motor neurons.

Materials and Methods

Drosophila *husbandry*

Flies were reared at 21°C on standard fly food (1 l of food contained: 95 g of agar, 275 g of Brewer's yeast, 520 g of cornmeal, 110 g of sugar, 45 g of propionic acid, and 36 g of Tegosept) unless otherwise stated. The following fly lines were obtained from Bloomington *Drosophila* Stock Center: *ok371-GAL4* and *d42-GAL4* (Parkes et al., 1998; Mahr and Aberle, 2006), RyR^{16} (Sullivan et al., 2000), *UAS-Dcr1* (Dietzl et al., 2007), *UAS-CKII-I.Ala* ($UAS\text{-}CKII^{ala}$; Joiner and Griffith, 1997), *UAS-mCherry-mito-OMM* (Vagnoni and Bullock, 2016), and $UAS\text{-}itpr^{RNAi}$ (*TRiP.JF01957*; Wong et al., 2021). Other strains used in the study were: $UAS\text{-}vapb^{WT}$ and $UAS\text{-}vapb^{P58S}$ (Tsuda et al., 2008), *UAS-GCaMP5G-tdTomato* (Wong et al., 2021), *Canton-S*, *UAS-PercevalHR* (Wong et al., 2021), iav^{1} (also called $iav^{hypoB\text{-}1}$; Wong et al., 2014), and *UAS-iav* (Wong et al., 2014). *Canton-S* flies were used as the wild-type controls in the various crosses.

Analysis of RNAi-mediated gene knock-down

Flies expressing the relevant RNAi transgenes or *UAS-Luc* under the control of heat shock–inducible promoter (*hs-GAL4*) and *hs-GAL4*/+ controls were heat shocked on three consecutive days by placing them in a 37°C water bath for 1-h each time. The day after the third heat shock, RNA was extracted from whole-fly extracts using RNeasy mini kit (QIAGEN) by following the manufacturer's instructions. Using the high-capacity cDNA reverse transcription kit (Applied Biosystems), 1 μg of total RNA was reverse-transcribed. Real-time qPCR was performed using PowerUP SYBR Green Master Mix (Applied Biosystems) by following the manufacturer's instructions. The primers used were as follows:

RpL32 forward: TACAGGCCCAAGATCGTGAA
RpL32 reverse: TCTCCTTGCGCTTCTTGGA
vapb (*Vap33*) forward: TGAAGTGCGTTTTCGAGATGC
vapb (*Vap33*) reverse: CTGAGCTAGTATTGGCACCCG

Neuromuscular junction (NMJ) immunohistochemistry and confocal microscopy

Dissection and immunostaining of NMJ was performed as described previously (Wong et al., 2014, 2015). Briefly, wandering third instar larvae were filleted in ice-cold PBS to remove all visceral organs except the brain and nerves. For microtubule staining, larvae were dissected in HL-3 (70 mM NaCl, 5 mM KCl, 1 mM $CaCl_2$, 20 mM $MgCl_2$, 10 mM $NaHCO_3$, 115 mM sucrose, 5 mM trehalose, and 5 mM HEPES; pH 7.2), before treated with HL-3 containing 50 μM nocodazole or 0.1% DMSO for 30 min at room temperature. The fillets were fixed in 4% paraformaldehyde in PBS for 30 min. The fixed fillets were washed with 0.1% Triton X-100 in PBS before incubation with primary antibodies overnight at 4°C. Primary antibody dilutions were 1:100 mouse anti-discs large (DLG), 1:50 mouse anti-Futsch, and 1:200 mouse anti-α-tubulin. The monoclonal antibodies against DLG (4F3), Futsch (22C10), and α-tubulin (12G10) were obtained from the Developmental Studies Hybridoma Bank (DSHB) developed under the auspices of the NICHD and maintained by The University of Iowa, Department of Biology, Iowa City, IA 52 242. The samples were then washed and probed with 1:200 FITC-conjugated anti-HRP (Jackson ImmunoResearch) and Alexa Fluor 568-conjugated anti-mouse secondary antibodies (ThermoFisher) at room temperature for 1.5 h, and then mounted on glass slides with Vectashield (Vector Labs). Confocal images were obtained using a Nikon A1 Confocal Laser Microscope System (Nikon). For NMJ bouton counting, a 60× oil objective was used to focus on the NMJs on abdominal segment 3.

To count the number of microtubule loops within the type 1b NMJ boutons in larvae stained with anti-α-tubulin antibody, we applied an HRP mask to remove the α-tubulin signal outside the boutons. Briefly, confocal images were opened in the Fiji image processing package. We first separated the merged Z-stacks into the anti-HRP and anti-tubulin channels. Next, we applied the "Make Binary" function to the anti-HRP channel using default settings, and having checked "Calculate threshold for each image" and "Black background (of binary masks)." We then generated a maximum intensity Z-projection of the binary image, and inverted the color to generate the mask. Using the "Image Calculator"

dialogue window, we subtracted the mask from the anti-α-tubulin stack to remove the anti-α-tubulin signal outside the boutons.

To analyze mitochondria within NMJ boutons, we first separated merged Z-stack images into the mCherry-mito-OMM and anti-HRP signals. We generated an HRP mask exactly as described above to remove any mCherry signal outside the NMJs. To determine the number, volume, and surface area of the mitochondria at the NMJ, we used the "3D Object Counter v2.0" dialogue box with "Threshold" set at 50 and minimum "Size filter" set to 1. We then determined the aspect ratio (volume/surface area ratio) for each entity identified by the software. Operating under the assumption that the aspect ratio of each mitochondrion should be distinct, akin to a fingerprint, we filtered out all the counted particles whose aspect ratio was duplicated in the dataset for that NMJ. The remaining particles were counted in the analyses.

Larval crawling assay

Larval crawling assay was performed as reported previously (Kashima et al., 2017). Briefly, a 100 mm Petri dish half-filled with 2% agar was placed on an LED drawing pad in a dark room. A black paper strip was wrapped around the circumference of the Petri dish to form a 20-mm-tall wall. Late third-instar larvae were collected from fly food-containing vials, briefly rinsed with water, and placed in a 35-mm Petri dish. A paint brush was used to transfer one larva to the center of the agar plate. A digital camera connected to a laptop computer was mounted at ~80 cm above the Petri dish to capture time-lapse images at 2-s intervals (0.5 frame per second). Image recording continued until the larva reached the perimeter of the dish or for a maximum of 5 min. We used each larva in the assay only once. For analysis, we superimposed the time-lapse images of every 10 s (five frames) using ImageJ (NIH). A translucent ruler with millimeter marks on the LED pad was used as calibration scale. Position of each larva was tracked on the superimposed image to measure the total crawling distance in millimeters. Mean velocity was calculated by dividing the distance by the duration of the time. At least six larvae were recorded and analyzed for each genotype.

NMJ electrophysiology

Wandering third instar larvae were dissected in ice-cold HL-3 (70 mM NaCl, 5 mM KCl, 20 mM $MgCl_2.6H_2O$, 10 mM $NaHCO_3$, 115 mM sucrose, 5 mM trehalose, and 5 mM HEPES; pH 7.2) and rinsed with HL-3 containing 0.5 mM Ca^{2+}. Recordings were made from body-wall muscle 6 (abdominal segment 3) with sharp electrodes filled with a 2:1 mixture of 2 M potassium acetate and 2 M potassium chloride. Data were collected from samples with resting membrane potential below −60 mV. Excitatory postsynaptic junctional potentials (EJPs) were evoked by directly stimulating the A3 hemisegmental nerve through a glass capillary electrode (internal diameter, ~10 μm) at 0.2 Hz. Stimulus pulses were generated by pClamp 10 software (Molecular Devices Inc). The applied currents were 6 $\pm$3 μA with fixed stimulus duration at 0.3 ms. A total of 20–30 evoked EJPs were recorded for each muscle for analysis. Miniature EJP (mEJP) events were collected for 5 min. Both EJPs and mEJPs were amplified with an Axoclamp 900A amplifier (Molecular Devices) under bridge mode, filtered at 10 kHz and digitized at 10 kHz (EJPs) and 40 kHz (mEJPs) with pClamp 10. Experiments were performed at 21°C. EJPs and paired-pulse stimulation were analyzed with pClamp 8.0 software (Molecular Devices). The mEJPs were analyzed using the Mini Analysis Program (Synaptosoft Inc.). The EJPs paired-pulse amplitudes were corrected by nonlinear summation (Feeney et al., 1998). Paired-pulse ratio was calculated as the ratio of second to first peak. The quantal content of evoked release was calculated from individual muscles by the ratio of the average EJP amplitude over the average mEJP amplitude. For high-frequency stimulation, nerves were stimulated for 10 min at 10 Hz. By fitting the decay portions of each high-frequency trace to first order exponential function, we obtained the rate constant of decays. Rundowns were extracted from the rate-constants of decay.

Dissociation of Drosophila *neurons*

We dissociated primary motor neurons from *Drosophila* as described previously (Wong et al., 2021). Briefly, the exterior of wandering third instar larvae was sterilized by brief submersion in ethanol, and then washed with sterilized H_2O before dissection in filtered Schneider's medium (S0146; Sigma-Aldrich) containing 10% fetal bovine serum (FBS), antibiotic/antimycotic solution (A5955; Sigma-Aldrich) and 50 μg/ml of insulin (I6634; Sigma-Aldrich). Brains dissected from these larvae were washed in separate wells containing filtered Schneider's medium before being transferred to a filtered HL-3 solution (70 mM NaCl, 5 mM KCl, 1 mM $CaCl_2$, 20 mM $MgCl_2$, 10 mM $NaHCO_3$, 115 mM sucrose, 5 mM trehalose, and 5 mM HEPES) supplemented with 0.423 mM L-cysteine (Calbiochem) and 5 U/ml papain (Worthington; note, after L-cysteine addition but before papain addition, the pH of the solution was recalibrated to 7.4). The brains were then enzymatically digested in the papain solution for 20 min before transfer to a 1.5-ml tube containing 1 ml of filtered Schneider's medium. Cells were centrifuged at 100 G for 1 min before decantation of Schneider's medium. The solution was replaced with 1 ml of fresh filtered Schneider's medium. This process was repeated twice before neurons were dissociated by pipetting repeatedly until the solution was homogeneous. The solution with dissociated neurons was then placed on 35-mm glass bottom dishes (D35-10-0-N; Cellvis) that had been coated with concanavalin A (C2010; Sigma-Aldrich). Cells were cultured in Schneider's medium supplemented with 10% FBS, antibiotic/antimycotic solution (A5955; Sigma-Aldrich) and 50 μg/ml of insulin (I6634; Sigma-Aldrich) at room temperature in a humidified container at room temperature. After each day in culture, cells were washed with PBS to remove any yeast contamination or debris remaining from dissociation.

Live-cell imaging of fly primary neurons

Live imaging of dissociated neurons was performed as described previously (Wong et al., 2021). Briefly, culture media on plates of dissociated neurons was first replaced with HL-3 (70 mM NaCl, 5 mM KCl, 1 mM $CaCl_2$, 20 mM $MgCl_2$, 10 mM $NaHCO_3$, 115 mM sucrose, 5 mM trehalose, and 5 mM HEPES; pH 7.2, room temperature). For measurements of cytosolic Ca^{2+}, GCaMP5G and tdTomato were sequentially excited at 488 and 561 nm, respectively, by an A1 laser confocal microscope with a 40× objective (Nikon). Emission signals at 525 and 595 nm were recorded. Backgrounds were measured from a cell-free region of interest (ROI). Baselines were established for 1 min before addition of muscarine (1 mM). Cytosolic Ca^{2+} transients were evoked by store-depletion with the SERCA inhibitor, thapsigargin (TG), as described. Amplitudes of the GCaMP5G/tdTomato ratio represented cytosolic free [Ca^{2+}]. More than 50 cells from a minimum of three independently conducted experiments for each condition were used for the calculations.

PercevalHR signals were recorded by measuring the ratio of fluorescence emissions at 525 nm sequentially excited at 487.5 and 407.8 nm. An A1R laser confocal microscope with 40× objective (Nikon) was used for measurement. Background emission signals were measured from a cell-free ROI. Baselines were established for 2 min before the bath was replaced with high [K^+] (52 mM) HL-3. Oligomycin A (oligoA; 10 μM) were added as needed and signals were recorded. Amplitudes of the emission ratio represented the cytosolic [ATP]/[ADP] ratio (Tantama et al., 2013; Wong et al., 2021). Data were quantified as change in the PercevalHR ratio over the baseline that was set to the value at the time point immediately before the addition of the drug. We determined the cumulative change in the ratio using a custom R code and the area under the curve (AUC) per unit time. Cells from a minimum of three to four independently conducted experiments for each condition were used for the calculations.

Analysis of fly lifespan

Newly eclosed adult flies of both sexes were collected and transferred to vials containing standard fly food (≤15 flies per vial). Flies were kept at room temperature (~21°C) and transferred to new vials twice per week. Dead flies at the bottom of the old vials were counted after each transfer until all the animals in a cohort died.

Experimental design and statistical analyses

Excel (Microsoft), and Prism 8 (GraphPad) were used for statistical analyses and curve-fitting. We used either parametric or nonparametric tests

of statistical significance on the basis of whether the data were normally distributed. We assessed the normality of data using the Shapiro-Wilk test. Descriptions of the data distribution are provided in the tables. Multiple comparisons were made by ANOVA or Kruskal–Wallis tests. Custom R code used for quantifying [Ca^{2+}] and PercevalHR data. Statistical significance was defined as a $p < 0.05$. *P*-values were shown on the figures as asterisks: $^{*}p < 0.05$, $^{**}p < 0.01$, $^{***}p < 0.001$, $^{****}p < 0.0001$. Lifespan (Kaplan–Meier) curves were generated using Prism 8. We used the log-rank (Mantel–Cox) test to determine *p*-values. Other test-specific values are provided in the tables.

Results

Expression of an ALS-related variant of *vapb* results in defective presynaptic bouton development

Either the deletion of *Drosophila vapb* (also called *Vap33*) or the expression of a transgene equivalent to an ALS-causing variant ($vapb^{P58S}$) disrupts presynaptic microtubules at the larval NMJ resulting in the appearance of fewer, but morphologically larger, boutons (Pennetta et al., 2002; Chai et al., 2008; Ratnaparkhi et al., 2008). We confirmed that in comparison to the *GAL4* and *UAS* controls, ectopic expression of $vapb^{P58S}$, but not wild-type *vapb* ($vapb^{WT}$), in motor neurons (using $VGlut^{ok371}$-*GAL4*, herein referred to as *ok371-GAL4*) led to a significant reduction in bouton number (Fig. 1*A–E*; Brand and Perrimon, 1993; Mahr and Aberle, 2006; Tsuda et al., 2008). NMJ boutons in neurons expressing $vapb^{P58S}$ also exhibited significant increases in bouton area (Fig. 1*A,B,F*). Although animals expressing $vapb^{WT}$ in motor neurons exhibited a slight, yet significant, increase in bouton area (Fig. 1*D,F*) relative to the *UAS* controls, bouton numbers in these animals were not significantly altered (Fig. 1*E*). Animals expressing $vapb^{P58S}$, however, exhibited significantly fewer and larger boutons in relation to the *GAL4/UAS* controls and those expressing $vapb^{WT}$ (Fig. 1*E,F*). These data agree with prior findings regarding the effects of $VAPB^{P58S}$ on *Drosophila* larval NMJ synapse morphology (Chai et al., 2008; Ratnaparkhi et al., 2008).

$VAPB^{P58S}$-induced defects in presynaptic bouton development are ameliorated by lowering the expression of genes encoding ER Ca^{2+} release channels

We previously showed that decreased abundance of ER Ca^{2+} release channels, Inactive (Iav), ryanodine receptor (RyR), and inositol trisphosphate receptor (IP_3R), result in NMJs that exhibit fewer boutons that are larger in size (Fig. 2*A*; Wong et al., 2014). The ostensible similarities between the morphology of NMJ boutons in iav^{1} mutants (also called $iav^{hypoB\text{-}1}$, strong hypomorphs of *iav*; Homyk and Sheppard, 1977; Wong et al., 2014) and animals expressing $vapb^{P58S}$ implies a common underlying mechanism. Therefore, we speculated that the coincidence of iav^{1} and $vapb^{P58S}$ would enhance the respective phenotypes leading to an even greater reduction in bouton number (Fig. 2*A*). To our surprise, expression of $vapb^{P58S}$ in the iav^{1} background restored, rather than worsened, both bouton number and morphology to control levels (Fig. 2*B,C,J,K*). Whereas bouton numbers and area elicited by $vapb^{P58S}$ were not significantly different from those in iav^{1}, these parameters were restored to wild-type levels on the coincidence of $vapb^{P58S}$ and iav^{1} (Fig. 2*J,K*). In contrast, overexpression of $vapb^{WT}$ did nothing to alter the paucity of boutons in iav^{1} (Fig. 2*D,E,L*). Therefore, decreased abundance of Iav rescued the synaptic growth phenotype stemming from the expression of $vapb^{P58S}$.

Next, we asked whether the rescue of $vapb^{P58S}$-induced NMJ phenotypes was specific to the loss of Iav, or whether similar suppression would occur in response to lowered abundance of other

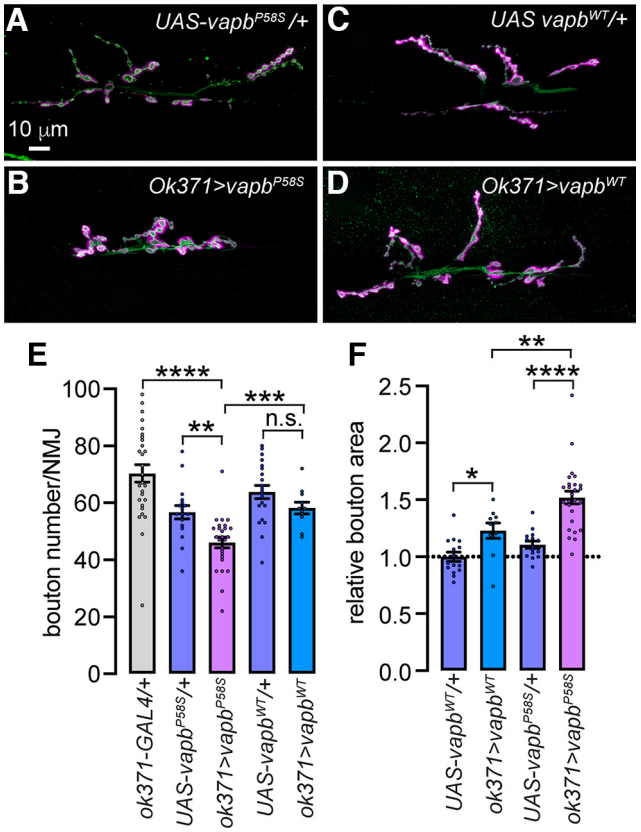

Figure 1. Expression of $vapb^{P58S}$ in *Drosophila* motor neurons led to significant changes in presynaptic bouton development at the larval NMJ. ***A–D***, Representative confocal images of larval NMJs dissected from animals of the indicated genotypes stained with antibodies against HRP (green) and DLG (magenta). Scale bar shown in ***A*** on the top left applies to all panels. Please note that in all figures, *UAS-transgene*/+ refers to the presence of the noted *UAS-transgene* construct without a *GAL4* driver, and *driver>transgene* refers to the *UAS-transgene*, whose expression was driven using the *driver-GAL4*. ***E***, ***F***, Bar graphs showing quantification of the larval NMJ bouton numbers (***E***) and relative bouton area (***F***) in animals of the indicated genotypes. Values represent mean ± SEM; $^{*}p < 0.05$, $^{**}p < 0.01$, $^{***}p < 0.001$, $^{****}p < 0.0001$; n.s., not significant, *t* tests with Bonferroni correction. Dots represent values from distinct NMJs. Refer to Table 1 for statistical information.

ER Ca^{2+} channels. Simultaneous knock-down of the gene encoding the fly IP_3R (*itpr*) using the *d42-GAL4* motor neuron driver and a validated RNAi line (*UAS-*$itpr^{RNAi}$) ameliorated the effect of $vapb^{P58S}$ expression on bouton number (Fig. 2*G,M*; Venkatesh and Hasan, 1997; Parkes et al., 1998; Wong et al., 2014, 2021). The *d42-GAL4*/+ and *UAS-*$vapb^{P58S}$/+ control animals did not exhibit a decrease in bouton numbers (Fig. 2*M*). Absence of comparable suppression in animals coexpressing $vapb^{P58S}$ and a neutral *UAS* transgene (*UAS-Dcr1*; Fig. 2*F,M*) demonstrates that the suppression brought about by coexpression of $itpr^{RNAi}$ was not because of GAL4 dilution stemming from the presence of a second *UAS* transgene. Concomitant absence of one copy of *RyR* (RyR^{16}/+), which mimics the iav^{1} NMJ growth phenotype, also prevented $vapb^{P58S}$-induced alterations in bouton numbers (Fig. 2*H,I,N*; Sullivan et al., 2000; Wong et al., 2014). Taken together, these data demonstrate that $VAPB^{P58S}$-induced defects in presynaptic bouton development are ameliorated by cell autonomous reduction in the expression of genes encoding ER Ca^{2+} channels.

CaMKII overactivation underlies alterations in presynaptic development in motor neurons expressing $vapb^{P58S}$

The aforementioned findings are consistent with the notion of $VAPB^{P58S}$ inducing an increase in cytosolic [Ca^{2+}] such that the

Table 1. Statistical information for the data shown in Figure 1

Figure 1*E*

Genotype	Normally distributed?	Values	Number of animals
ok371-GAL4/+	Yes	70.3 ± 3.1	14 (*n* = 28 NMJs)
UAS-vapb^{P58S}/+	Yes	56.7 ± 2.4	9 (*n* = 17 NMJs)
ok371>vapb^{P58S}	Yes	46.1 ± 1.9	13 (*n* = 26 NMJs)
UAS-vapb^{WT}/+	Yes	63.8 ± 2.3	11 (*n* = 21 NMJs)
ok371>vapb^{WT}	Yes	58.2 ± 2.0	6 (*n* = 11 NMJs)

Comparison between	Test used	*P*-value	Test statistics
ok371-GAL4/+ ok371>vapb^{P58S}	*t* test followed by Bonferroni correction	0.0039	*t* = 3.519, df = 33.74
UAS-vapb^{P58S}/+ ok371>vapb^{P58S}	*t* test followed by Bonferroni correction	0.0024	*t* = 3.767, df = 28.97
ok371>vapb^{P58S} ok371>vapb^{WT}	*t* test followed by Bonferroni correction	0.0006	*t* = 4.379, df = 26.47
UAS-vapb^{WT}/+ ok371>vapb^{WT}	*t* test followed by Bonferroni correction	0.24	*t* = 1.807, df = 28.68

Figure 1*F*

Genotype	Normally distributed?	Values	Number of animals
UAS-vapb^{WT}/+	Yes	1 ± 0.04	8 (*n* = 15 NMJs)
ok371>vapb^{WT}	Yes	1.23 ± 0.07	5 (*n* = 10 NMJs)
UAS-vapb^{P58S}/+	Yes	1.11 ± 0.03	8 (*n* = 16 NMJs)
ok371>vapb^{P58S}	No	1.52 ± 0.06	13 (*n* = 26 NMJs)

Comparison between	Test used	*P*-value	Test statistics
UAS-vapb^{WT}/+ ok371>vapb^{WT}	*t* test followed by Bonferroni correction	0.02	*t* = 2.901, df = 15.24
ok371>vapb^{WT} ok371>vapb^{P58S}	Mann–Whitney followed by Bonferroni correction	0.0096	*U* = 27
UAS-vapb^{P58S}/+ ok371>vapb^{P58S}	Mann–Whitney followed by Bonferroni correction	<0.0001	*U* = 27

attenuation of ER Ca^{2+} release restores homeostasis, and thus, mitigates the bouton development phenotypes. Our data also imply that either an increase or decrease in presynaptic [Ca^{2+}] results in morphologically identical bouton phenotypes. Indeed, we previously showed that either the absence or overexpression of *iav* results in comparable reduction in the number of NMJ boutons (Wong et al., 2014). How might this bell-shaped relationship between presynaptic [Ca^{2+}] and NMJ bouton development come about?

We posit that the key to understanding these outcomes is the stability of presynaptic microtubules. We and others have shown that destabilization of presynaptic microtubules, which manifests as loss of characteristic intrabouton microtubule loops, results in an increase bouton size, and a concomitant decrease in bouton number (Roos et al., 2000; Pennetta et al., 2002; Viquez et al., 2006; Wong et al., 2014). Indeed, the number of presynaptic microtubule loops at NMJs of animals expressing *vapb^{P58S}* in motor neurons was significantly lower than that in animals expressing *vapb^{WT}* (Fig. 3*A*,*B*). Treatment of NMJs with the microtubule depolymerizing agent, nocodazole, led to a reduction in the number of microtubule loops at the NMJs of animals expressing *vapb^{WT}*, whereas we observed no further decrease in the number of microtubule loops in nocodazole-treated NMJs in animals expressing *vapb^{P58S}* (Fig. 3*A*,*B*). The number of microtubule loops in nocodazole-treated *vapb^{WT}* NMJs was statistically indistinguishable from those in nocodazole-treated or -untreated *vapb^{P58S}* NMJs (Fig. 3*B*). These data are consistent with microtubule depolymerization underlying the fewer microtubule loops within the *vapb^{P58S}* NMJs.

We showed previously that reduction in presynaptic resting [Ca^{2+}] and the attendant attenuation of the Ca^{2+}/calmodulin (CaM) responsive phosphatase, calcineurin (CanA1), destabilize presynaptic microtubules (Wong et al., 2014). In the event of a Ca^{2+}-responsive kinase having the same target as CanA1, increased activity of that kinase could also result in hyperphosphorylation of the target. If so, one might expect that either an increase or decrease in cytosolic [Ca^{2+}] would result in higher fractions of that target being phosphorylated. Since activation of the Ca^{2+}/CaM-dependent protein kinase II (CaMKII or CKII) by high [Ca^{2+}] destabilizes microtubules by phosphorylating microtubule-associated proteins (MAPs; Baratier et al., 2006; McVicker et al., 2015; Oka et al., 2017), we asked whether elevated ER Ca^{2+} release compels the observed changes in NMJ development because of unrestrained CaMKII activity. Mirroring the decrease in the number of presynaptic microtubule loops, NMJs in animals expressing *vapb^{P58S}* also exhibited fewer loops of the fly MAP1b homolog, Futsch (Hummel et al., 2000; Roos et al., 2000; Fig. 3*C*,*D*). Coexpression of the CaMKII inhibitory peptide, CaMKII^{ala} (CKII^{ala}; Joiner and Griffith, 1997), with *vapb^{P58S}* led to recovery of the numbers of Futsch loops (Fig. 3*C*,*D*) and boutons (Fig. 3*E*). In *iav^{1}* synapses, which exhibit lower resting [Ca^{2+}] (Wong et al., 2014), expression of *CKII^{ala}* did not restore the bouton number (Fig. 3*E*). Suggesting a specific rescue of the *vapb^{P58S}* phenotype rather than a general increase in bouton number, overexpression of *CKII^{ala}* without *vapb^{P58S}* was not sufficient to elevate the number of presynaptic boutons (Fig. 3*E*). Indicating the sufficiency of CaMKII downstream of elevated [Ca^{2+}], in *iav*-overexpressing neurons, which exhibit higher presynaptic [Ca^{2+}] (Wong et al., 2014), bouton number was restored to wild-type level on coexpression of *CKII^{ala}* (Fig. 3*F*). Taken together, these data suggest a biphasic dependency of presynaptic microtubule stability and bouton number on cytosolic [Ca^{2+}], and that *vapb^{P58S}*-induced alterations in presynaptic development stem from aberrant CaMKII activation (Fig. 3*G*).

Next, we asked whether *vapb^{P58S}*-induced phenotypes other than NMJ development also stem from elevated presynaptic [Ca^{2+}] and CaMKII activation. Since *vapb^{P58S}* is equivalent to the ALS-causing variant of human *VAPB* (Nishimura et al., 2004, 2005; Kanekura et al., 2006; Marques et al., 2006; Landers et al., 2008), we examined locomotor activity in larvae expressing

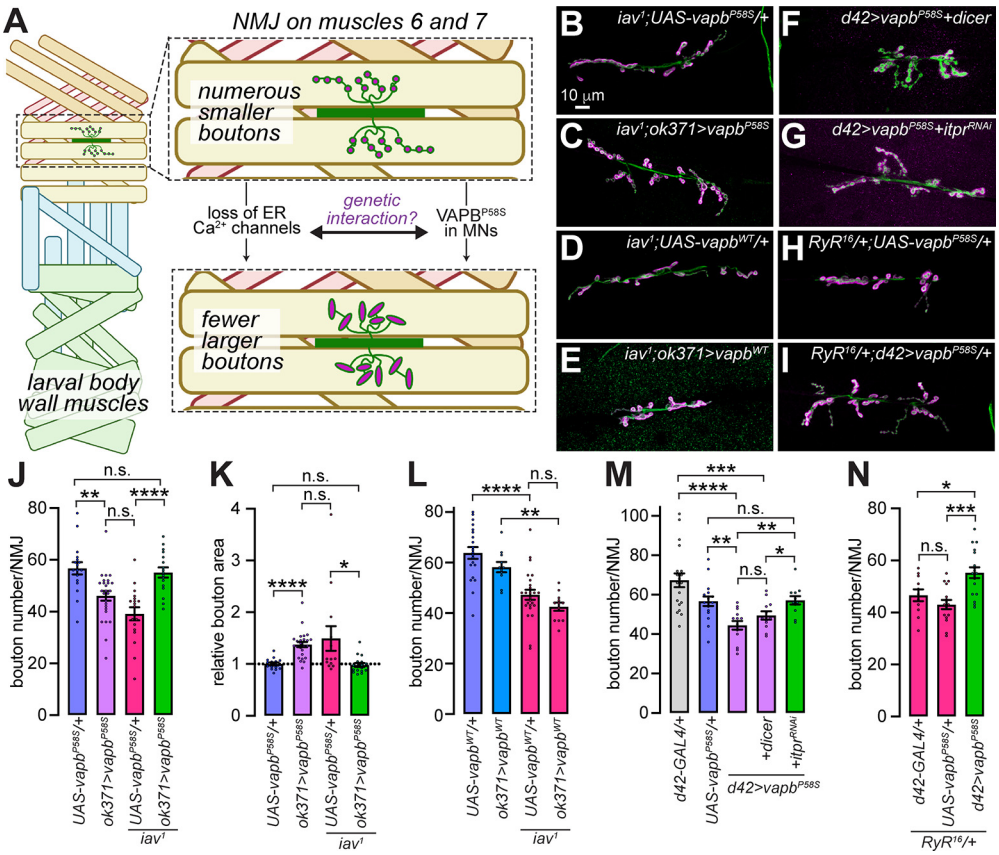

Figure 2. VAPB^{P58S}-induced defects in presynaptic bouton development are ameliorated on concomitant loss of ER Ca^{2+} release channels. ***A***, Model showing that the development of control NMJs on muscles 6 and 7 of the larval body wall muscles leads to the appearance of numerous small boutons. Animals either expressing *vapb*^{P58S} in motor neurons or harboring mutations that diminish ER Ca^{2+} release are characterized by the appearance of fewer, but morphologically larger, boutons. Ostensible similarities in bouton development phenotypes raises the question of genetic interactions between these conditions. Image was created with BioRender. ***B–I***, Representative confocal images of larval NMJs dissected from animals of the indicated genotypes stained with antibodies against HRP (green) and DLG (magenta). Scale bar shown in ***B*** applies to all panels. ***J–N***, Bar graphs showing quantification of the larval NMJ bouton numbers (***J***, ***L–N***) and relative bouton area (***K***) in animals of the indicated genotypes. Values represent mean ± SEM; *$p < 0.05$, **$p < 0.01$, ***$p < 0.001$, ****$p < 0.0001$; n.s., not significant, paired *t* tests with Bonferroni correction. Dots represent values from distinct NMJs. Quantification of bouton numbers in Figure 1 and this figure were from the same experiment. Refer to Table 2 for statistical information.

this transgene in motor neurons. To this end, we placed wandering third instar larvae in an open field and recorded their movement toward the periphery of the field (Fig. 4*A*). In comparison to larvae expressing *vapb*^{WT}, those expressing *vapb*^{P58S} exhibited a significant reduction in velocity (Fig. 4*A*,*B*). Upon coexpression of either *itpr*^{RNAi} or *CKII*^{ala}, the velocities of *vapb*^{P58S}-expressing larvae were no longer significantly different from the animals expressing *vapb*^{WT} with *itpr*^{RNAi} or *CKII*^{ala}, respectively (Fig. 4*B*).

Expression of *vapb*^{P58S} in motor neurons shortens *Drosophila* lifespan via overactivation of PLCβ–IP$_3$R signaling, and either the deletion of the gene encoding a fly PLCβ (*norpA*; Bloomquist et al., 1988) or the concomitant knock-down of *itpr* strongly suppresses the effects of VAPB^{P58S} on animal longevity (Wong et al., 2021). In contrast to the ameliorative effects on the NMJ bouton phenotype, neither *iav*^{1} nor the *RyR*^{16}/+ mutations influenced the lifespan of animals expressing *vapb*^{P58S} (Wong et al., 2021). Therefore, the effects of *vapb*^{P58S} on NMJ bouton development and adult lifespan occur via distinct mechanisms. In agreement, coexpression of *CKII*^{ala}, which mitigated the NMJ growth and larval velocity phenotypes in animals expressing *vapb*^{P58S}, did not influence the effect of mutant VAPB on adult lifespan (Fig. 4*C*). Collectively, these data show that although larval phenotypes in *vapb*^{P58S}-expressing animals involves CaMKII, the same is not the case for adult longevity.

Expression of *vapb*^{P58S} results in diminished extrusion of cytosolic Ca^{2+}

Lower presynaptic resting [Ca^{2+}] in the absence of Iav results in reduced probability of synaptic vesicle (SV) release (Wong et al., 2014). NMJs in *iav*^{1} animals, therefore, exhibit reduced amplitudes of evoked EJPs and paired-pulse facilitation in response to a second stimulus applied after a delay of 50 ms (Wong et al., 2014). Conversely, overexpression of *iav* led to an increase in presynaptic resting [Ca^{2+}], higher EJP amplitudes, and paired-pulse depression indicating elevated SV release probability (Wong et al., 2014). These data point to a dose-dependent effect of ER Ca^{2+} release on presynaptic resting [Ca^{2+}] and SV release probability. Given that the NMJ bouton phenotypes in animals overexpressing either *vapb*^{P58S} or *iav* were suppressed by CKII^{ala}, we asked whether VAPB^{P58S} also elevates SV release probability because of an increase in resting [Ca^{2+}]. If so, expression of *vapb*^{P58S} would result in increased EJP amplitude and paired-pulse depression. However, EJP amplitudes in *vapb*^{P58S} neurons were not significantly different from those in *vapb*^{WT} neurons (Fig. 5*A*,*B*), which is in agreement with the report that ectopic expression of the ALS-causing human transgene (*hVAP*^{P56S}) had no effect on the amplitude of evoked potentials at the *Drosophila* larval NMJ (Chai et al., 2008). Furthermore, relative to neurons expressing *vapb*^{WT}, those expressing *vapb*^{P58S} showed paired-

Table 2. Statistical information for the data shown in Figure 2

Figure 2*J*

Genotype	Normally distributed?	Values	Number of animals
UAS-vapb^{P58S}/+	Yes	56.7 ± 2.4	9 (*n* = 17 NMJs)
ok371>vapb^{P58S}	Yes	46.1 ± 1.9	13 (*n* = 26 NMJs)
iav^{1};UAS-vapb^{P58S}/+	Yes	39.2 ± 2.6	9 (*n* = 18 NMJs)
iav^{1};ok371>vapb^{P58S}	Yes	55.1 ± 2	9 (*n* = 17 NMJs)

Comparison between	Test used	*P*-value	Test statistics
UAS-vapb^{P58S}/+ *ok371>vapb^{P58S}*	*t* test followed by Bonferroni correction	0.0024	*t* = 3.767, df = 28.97
UAS-vapb^{P58S}/+ *iav^{1};ok371>vapb^{P58S}*	*t* test followed by Bonferroni correction	1	*t* = 0.5174, df = 30.85
ok371>vapb^{P58S} *iav^{1};UAS-vapb^{P58S}/+*	*t* test followed by Bonferroni correction	0.12	*t* = 2.183, df = 33.57
iav^{1};UAS-vapb^{P58S}/+ *iav^{1};ok371>vapb^{P58S}*	*t* test followed by Bonferroni correction	<0.0001	*t* = 4.966, df = 31.30

Figure 2*K*

Genotype	Normally distributed?	Values	Number of animals
UAS-vapb^{P58S}/+	Yes	1 ± 0.03	8 (*n* = 15 NMJs)
ok371>vapb^{P58S}	No	1.37 ± 0.05	5 (*n* = 10 NMJs)
iav^{1};UAS-vapb^{P58S}/+	No	1.49 ± 0.24	7 (*n* = 13 NMJs)
iav^{1};ok371>vapb^{P58S}	No	0.98 ± 0.04	9 (*n* = 17 NMJs)

Comparison between	Test used	*P*-value	Test statistics
UAS-vapb^{P58S}/+ *ok371>vapb^{P58S}*	Mann–Whitney followed by Bonferroni correction	<0.0001	*U* = 27
UAS-vapb^{P58S}/+ *iav^{1};ok371>vapb^{P58S}*	Mann–Whitney followed by Bonferroni correction	0.9	*U* = 99
ok371>vapb^{P58S} *iav^{1};UAS-vapb^{P58S}/+*	Mann–Whitney followed by Bonferroni correction	0.6	*U* = 124
iav^{1};UAS-vapb^{P58S}/+ *iav^{1};ok371>vapb^{P58S}*	Mann–Whitney followed by Bonferroni correction	0.018	*U* = 46

Figure 2*L*

Genotype	Normally distributed?	Values	Number of animals
UAS-vapb^{WT}/+	Yes	63.8 ± 2.3	11 (*n* = 21 NMJs)
ok371>vapb^{WT}	Yes	58.2 ± 2.0	6 (*n* = 11 NMJs)
iav^{1};UAS-vapb^{WT}/+	Yes	42.5 ± 1.6	6 (*n* = 12 NMJs)
iav^{1};ok371>vapb^{WT}	Yes	47.2 ± 2.0	13 (*n* = 25 NMJs)

Comparison between	Test used	*P*-value	Test statistics
UAS-vapb^{WT}/+ *iav^{1};UAS-vapb^{WT}/+*	*t* test followed by Bonferroni correction	<0.0001	*t* = 7.535, df = 30.86
ok371>vapb^{WT} *iav^{1};ok371>vapb^{WT}*	*t* test followed by Bonferroni correction	0.0018	*t* = 3.853, df = 27.60
ok371>vapb^{P58S} *iav^{1};UAS-vapb^{P58S}/+*	*t* test followed by Bonferroni correction	0.21	*t* = 1.860, df = 33.96

Figure 2*M*

Genotype	Normally distributed?	Values	Number of animals
d42-GAL4/+	Yes	67.3 ± 3.5	10 (*n* = 20 NMJs)
UAS-vapb^{P58S}/+	Yes	56.7 ± 2.4	8 (*n* = 15 NMJs)
d42>vapb^{P58S}	Yes	44.5 ± 2.2	7 (*n* = 14 NMJs)
d42>vapb^{P58S}+dicer	Yes	49.5 ± 2.1	6 (*n* = 12 NMJs)
d42>vapb^{P58S}+itpr^{RNAi}	Yes	57.2 ± 2.1	6 (*n* = 12 NMJs)

Comparison between	Test used	*P*-value	Test statistics
d42-GAL4/+ *d42>vapb^{P58S}*	*t* test followed by Bonferroni correction	<0.0001	*t* = 5.507, df = 30.15
d42-GAL4/+ *d42>vapb^{P58S}+dicer*	*t* test followed by Bonferroni correction	0.0004	*t* = 4.368, df = 28.63
UAS-vapb^{P58S}/+ *d42>vapb^{P58S}*	*t* test followed by Bonferroni correction	0.0032	*t* = 3.767, df = 28.97
UAS-vapb^{P58S}/+ *d42>vapb^{P58S}+itpr^{RNAi}*	*t* test followed by Bonferroni correction	1	*t* = 0.1462, df = 26.92
d42>vapb^{P58S} *d42>vapb^{P58S}+dicer*	*t* test followed by Bonferroni correction	0.44	*t* = 1.647, df = 23.98
d42>vapb^{P58S} *d42>vapb^{P58S}+itpr^{RNAi}*	*t* test followed by Bonferroni correction	0.0012	*t* = 1.860, df = 33.96
d42>vapb^{P58S}+dicer *d42>vapb^{P58S}+itpr^{RNAi}*	*t* test followed by Bonferroni correction	0.04	*t* = 2.606, df = 22.00

Figure 2*N*

Genotype	Normally distributed?	Values	Number of animals
RyR^{16}/+;UAS-vapb^{P58S}/+	Yes	43.1 ± 1.8	8 (*n* = 16 NMJs)
RyR^{16}/+;d42-GAL4/+	Yes	46.6 ± 2.3	6 (*n* = 11 NMJs)
RyR^{16}/+;d42>vapb^{P58S}	Yes	55.3 ± 2.1	9 (*n* = 18 NMJs)

Comparison between	Test used	*P*-value	Test statistics
RyR^{16}/+;UAS-vapb^{P58S}/+ *RyR^{16}/+;d42-GAL4/+*	*t* test followed by Bonferroni correction	0.67	*t* = 1.246, df = 20.68
RyR^{16}/+;d42-GAL4/+ *RyR^{16}/+;d42>vapb^{P58S}*	*t* test followed by Bonferroni correction	0.0003	*t* = 4.430, df = 32
RyR^{16}/+;UAS-vapb^{P58S}/+ *RyR^{16}/+;d42>vapb^{P58S}*	*t* test followed by Bonferroni correction	0.027	*t* = 2.813, df = 23.92

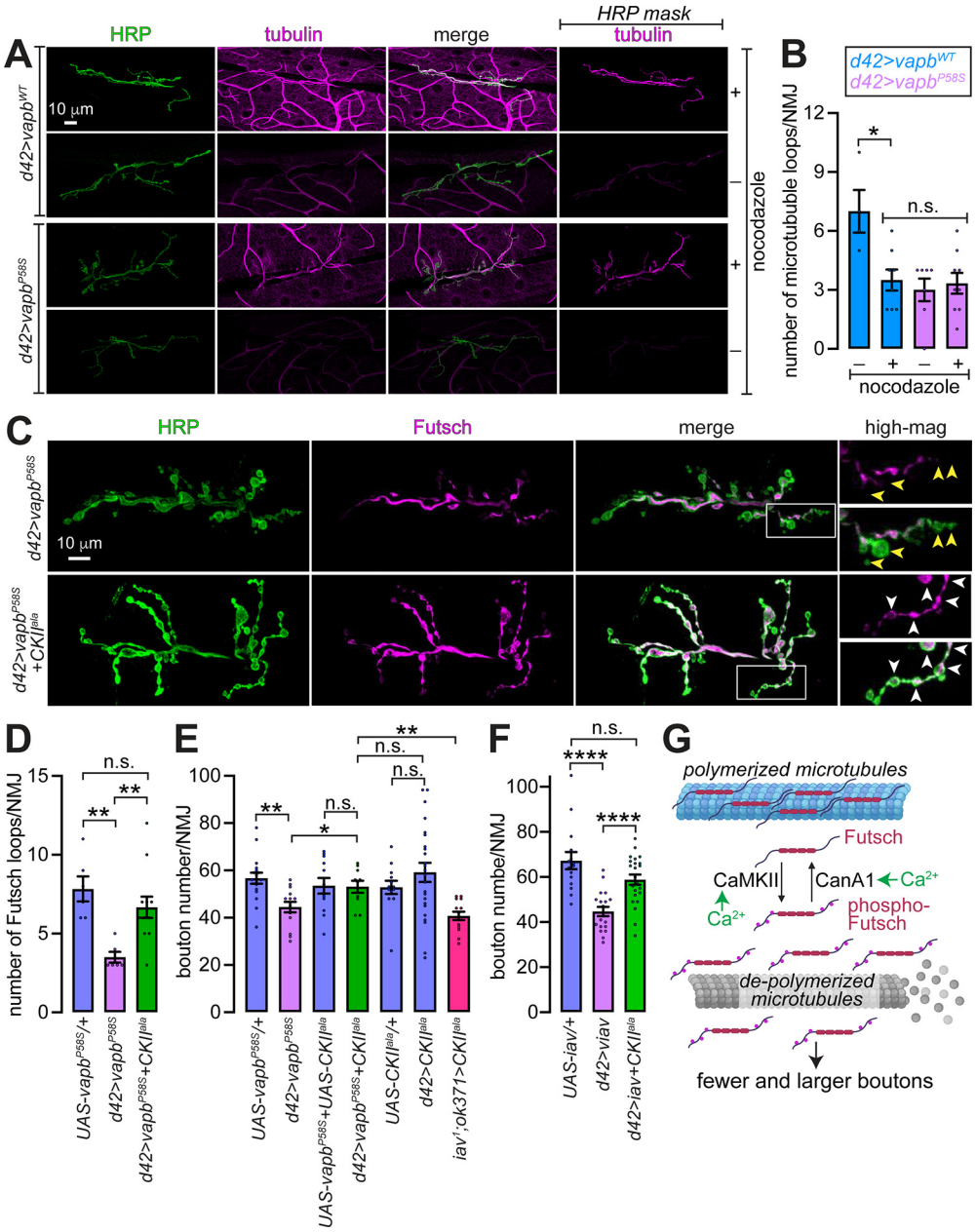

Figure 3. CaMKII underlies the alterations in presynaptic bouton development in motor neurons expressing $vapb^{P58S}$. ***A***, Representative confocal images of larval NMJs dissected from animals of the genotypes indicated on the left, stained with antibodies against HRP (green) and tubulin (magenta) as indicated on the top. Images derived by application of an HRP mask to the anti-tubulin images are shown. Whether or not the larvae were treated with nocodazole is indicated with + or – on the right. Scale bar shown in top left image applies to all the images in the panel. ***B***, Bar graph showing quantification of the number of microtubule loops within each NMJ. Values represent mean ± SEM; $*p < 0.05$; *t* tests; and n.s., not significant, Kruskal–Wallis. Dots represent values from distinct NMJs. ***C***, Representative confocal images of NMJs expressing $vapb^{P58S}$ either with or without $CKII^{ala}$ as indicated. Samples were stained with antibodies against HRP (green) and Futsch (magenta). White arrowheads point to individual boutons and highlight recovery of Futsch loops in neurons expressing both $vapb^{P58S}$ and $CKII^{ala}$. Higher magnification images (high-mag) represent the regions shown in the box overlaid on the merged images. Scale bar shown on the top left applies to all panels. ***D–F***, Bar graphs showing quantification of the number of Futsch loops per NMJ (***D***) and larval NMJ bouton numbers (***E***, ***F***) in animals of the indicated genotypes. Values represent mean ± SEM; $*p < 0.05$, $**p < 0.01$, $****p < 0.0001$; n.s., not significant, paired *t* tests with Bonferroni correction. Dots represent values from distinct NMJs. Quantification of bouton numbers in Figures 1 and 2 and this figure were from the same experiment. ***G***, Model showing that either an increase or decrease in presynaptic $[Ca^{2+}]$ could result in Futsch hyperphosphorylation and depolymerization of presynaptic microtubules. Elevated $[Ca^{2+}]$ would lead to persistent activation of CaMKII, which could induce Futsch phosphorylation and attendant disruption of presynaptic microtubules leading to the appearance of fewer, but larger, boutons. Decreased expression of ER Ca^{2+} channels results in lower presynaptic resting $[Ca^{2+}]$ and diminished calcineurin activity (Wong et al., 2014), which also results in Futsch phosphorylation and attendant disruption of presynaptic microtubules leading to the appearance of fewer, but larger, boutons. Image was created with BioRender. Refer to Table 3 for statistical information.

pulse facilitation, rather than paired-pulse depression (Fig. 5*A*,*C*). Amplitudes of mini-EJPs (mEJPs) and quantal content were also virtually identical in $vapb^{WT}$-expressing and $vapb^{P58S}$-expressing NMJs (Fig. 5*D*,*E*). Taken together, these data argue against elevations in presynaptic resting $[Ca^{2+}]$ and SV release probability in $vapb^{P58S}$-expressing motor neurons.

What then could explain the hallmarks of elevated $[Ca^{2+}]$ in $vapb^{P58S}$-expressing motor neurons? Elevations in cytosolic $[Ca^{2+}]$ could stem either from greater Ca^{2+} influx or from

Table 3. Statistical information for the data shown in Figure 3

Figure 3*B*

Genotype	Normally distributed?	Values	Number of animals
d42>vapb^{WT}	Yes	7.0 ± 1.1	2 (*n* = 4 NMJs)
d42>vapb^{WT} + nocodazole	Yes	3.5 ± 0.5	4 (*n* = 8 NMJs)
d42>vapb^{P58S}	No	3.0 ± 0.6	4 (*n* = 7 NMJs)
d42>vapb^{P58S} + nocodazole	Yes	3.3 ± 0.5	5 (*n* = 10 NMJs)

Comparison between	Test used	*P*-value	Test statistics
d42>vapb^{WT} *d42>vapb^{WT}* + nocodazole	*t* test	0.03	*t* = 2.904, df = 4.533
d42>vapb^{WT} + nocodazole *d42>vapb^{P58S}* *d42>vapb^{P58S}* + nocodazole	Kruskal–Wallis	0.9379	Kruskal–Wallis statistic = 0.1282

Figure 3*D*

Genotype	Normally distributed?	Values	Number of animals
UAS-vapb^{P58S}/+	Yes	7.8 ± 0.8	3 (*n* = 6 NMJs)
d42>vapb^{P58S}	No	3.5 ± 0.3	3 (*n* = 6 NMJs)
d42>vapb^{P58S}+CKII^{ala}	Yes	6.7 ± 0.7	6 (*n* = 6 NMJs)

Comparison between	Test used	*P*-value	Test statistics
UAS-vapb^{P58S}/+ *d42>vapb^{P58S}*	Mann–Whitney followed by Bonferroni correction	0.006	*U* = 0
d42>vapb^{P58S} *d42>vapb^{P58S}+CKII^{ala}*	Mann–Whitney followed by Bonferroni correction	0.007	*U* = 5
UAS-vapb^{P58S}/+ *d42>vapb^{P58S}+CKII^{ala}*	*t* test followed by Bonferroni correction	0.84	*t* = 1.119, df = 12.06

Figure 3*E*

Genotype	Normally distributed?	Values	Number of animals
UAS-vapb^{P58S}/+	Yes	56.7 ± 2.4	8 (*n* = 15 NMJs)
d42>vapb^{P58S}	Yes	44.5 ± 2.2	7 (*n* = 14 NMJs)
UAS-vapb^{P58S}+UAS-CKII^{ala}	Yes	53.5 ± 3.3	6 (*n* = 12 NMJs)
d42>vapb^{P58S}+CKII^{ala}	Yes	53.1 ± 2.5	5 (*n* = 10 NMJs)
UAS-CKII^{ala}/+	No	52.9 ± 2.8	7 (*n* = 14 NMJs)
d42>CKII^{ala}	Yes	59.2 ± 4.0	12 (*n* = 24 NMJs)
iav^{1}; ok371 >CKII^{ala}	Yes	40.8 ± 1.8	7 (*n* = 14 NMJs)

Comparison between	Test used	*P*-value	Test statistics
UAS-vapb^{P58S}/+ *d42>vapb^{P58S}*	*t* test followed by Bonferroni correction	0.0032	*t* = 3.767, df = 28.97
d42>vapb^{P58S} *d42>vapb^{P58S}+CKII^{ala}*	*t* test followed by Bonferroni correction	0.03	*t* = 2.555, df = 19.88
UAS-vapb^{P58S}+UAS-CKII^{ala} *d42>vapb^{P58S}+CKII^{ala}*	*t* test followed by Bonferroni correction	1	*t* = 0.09618, df = 19.53
d42>vapb^{P58S}+CKII^{ala} *d42>CKII^{ala}*	*t* test followed by Bonferroni correction	0.6	*t* = 1.272, df = 32.00
d42>vapb^{P58S}+CKII^{ala} *iav^{1}; ok371 >CKII^{ala}*	*t* test followed by Bonferroni correction	0.003	*t* = 3.977, df = 17.07

Figure 3*F*

Genotype	Normally distributed?	Values	Test statistics
UAS-iav/+	Yes	67.3 ± 3.8	8 (*n* = 15 NMJs)
d42>iav	Yes	44.7 ± 2.1	10 (*n* = 19 NMJs)
d42>iav+CKII^{ala}	Yes	58.8 ± 2.2	12 (*n* = 23 NMJs)

Comparison between	Test used	*P*-value	Test statistics
UAS-iav/+ *d42>iav*	*t* test followed by Bonferroni correction	<0.0001	*t* = 5.214, df = 21.89
d42>iav *d42>iav+CKII^{ala}*	*t* test followed by Bonferroni correction	<0.0001	*t* = 4.611, df = 40.00
UAS-iav/+ *d42>iav+CKII^{ala}*	*t* test followed by Bonferroni correction	0.21	*t* = 1.907, df = 23.78

diminished Ca^{2+} extrusion from the cytosol. Since the former is ruled out by the aforementioned data, we asked whether the effects of $VAPB^{P58S}$ stem from diminished Ca^{2+} extrusion (Fig. 5*F*). We reasoned that diminished Ca^{2+} extrusion would promote the accumulation of residual Ca^{2+}, boost SV release in response to rapidly delivered stimuli, and thereby, explain the paired-pulse facilitation in *vapb^{P58S}*-expressing neurons (Fig. 5*A*, *C*). To examine the rates of Ca^{2+} extrusion, we performed live-cell imaging of larval motor neurons expressing GCaMP5G-tdTomato (Daniels et al., 2014; Wong et al., 2014, 2021). To ensure that our assessment of Ca^{2+} extrusion focused on transfer to the extracellular medium rather than uptake into the ER, we applied the SERCA inhibitor, TG (Lytton et al., 1991; Wong et al., 2021). Incidentally, TG-treatment evokes cytosolic Ca^{2+} transients because of leak of ER stores into the cytosol (Wong et al., 2021), and the kinetics of the return of these transients to baseline reflect the rate of Ca^{2+} extrusion. We found that the decay of TG-evoked GCaMP5G-tdTomato elevations followed a first order exponential function (Fig. 5*G*). Half-life of this decay was significantly higher in neurons expressing *vapb^{P58S}* compared with those expressing *vapb^{WT}* (Fig. 5*G*). These data argue in favor of diminished Ca^{2+} extrusion in neurons expressing *vapb^{P58S}*.

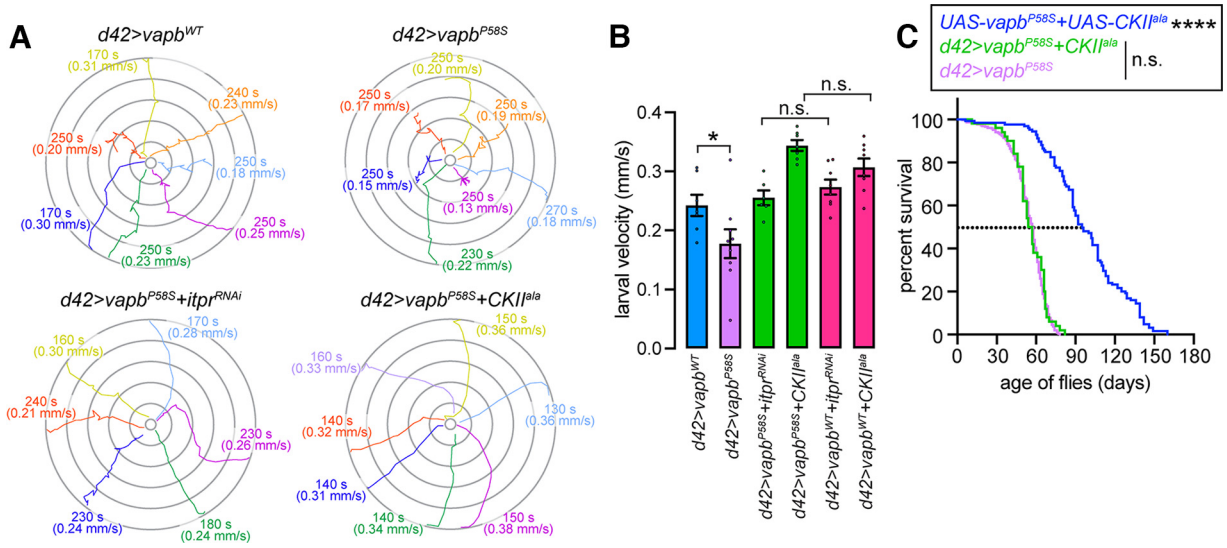

Figure 4. *vapb*^{P58S}-induced alterations in the velocity of larval peristalsis and adult longevity stem from overlapping and distinct underlying mechanisms. ***A***, Images showing the trajectory of larval crawling in an open field. Each colored line represents the path taken by distinct individual larvae. For each larva, duration for which video capture and mean velocity of crawling are noted. Genotypes of the larvae are indicated. ***B***, Bar graph showing quantification of crawling velocity of larvae of the indicated genotypes. Values represent mean ± SEM; *$p < 0.05$; n.s., not significant, *t* tests. Dots represent values from distinct larvae. ***C***, Lifespan of flies of the indicated genotypes; ****$p < 0.0001$; n.s., not significant, log-rank tests. Refer to Table 4 for statistical information.

Table 4. Statistical information for the data shown in Figure 4

Figure 4*B*

Genotype	Normally distributed?	Values	Number of animals
d42>vapb^{WT}	Yes	0.24 ± 0.02	7
d42>vapb^{P58S}	Yes	0.18 ± 0.02	9
d42>vapb^{P58S} + *itpr*^{RNAi}	Yes	0.23 ± 0.01	6
d42>vapb^{P58S} + *CKII*^{ala}	Yes	0.34 ± 0.01	7
d42>vapb^{WT} + *itpr*^{RNAi}	Yes	0.27 ± 0.01	8
d42>vapb^{WT} + *CKII*^{ala}	Yes	0.30 ± 0.01	8

Comparison between	Test used	*P*-value	Test statistics
d42>vapb^{WT} *d42>vapb*^{P58S}	*t* test	0.04	$t = 2.154$, df = 13.69
d42>vapb^{P58S} + *itpr*^{RNAi} *d42>vapb*^{WT} + *itpr*^{RNAi}	*t* test	0.3	$t = 1.024$, df = 11.78
d42>vapb^{P58S} + *CKII*^{ala} *d42>vapb*^{WT} + *CKII*^{ala}	*t* test	0.06	$t = 2.114$, df = 11.35

Figure 4*C*

Comparison between (number of animals)	Test used	*P*-value	Test statistics
UAS-vapb^{P58S} + *UAS-CKII*^{ala} (125) *d42>vapb*^{P58S} + *CKII*^{ala} (50) *d42>vapb*^{P58S} (350)	log-rank	<0.0001	$\chi^2 = 283.9$, df = 2
d42>vapb^{P58S} + *CKII*^{ala} (50) *d42>vapb*^{P58S} (350)	long-rank	0.5	$\chi^2 = 0.4$, df = 1

Rates of ATP production are unable to keep up with demand in *vapb*^{P58S}-expressing motor neurons

Electrochemical homeostasis in healthy neurons is maintained by pumps powered by mitochondrially-derived ATP (Fig. 6*A*). While SERCA and PMCA restore depolarization-induced changes in cytosolic [Ca^{2+}] to resting levels, the Na^+/K^+ ATPase restores the membrane potential (Fergestad et al., 2006; Chouhan et al., 2012; Ivannikov and Macleod, 2013; Le Masson et al., 2014). The purported coupling of ATP production to neuronal activity, therefore, ensures the availability of ATP for maintenance of Ca^{2+} homeostasis and for membrane repolarization (Fig. 6*A*, left; Le Masson et al., 2014; Rangaraju et al., 2014; Wong et al., 2021). In ALS neurons, defects in mitochondrial function are predicted to result in a paucity of ATP, which in turn, attenuates the activity of Ca^{2+} and Na^+/K^+ ATPases (Fig. 6*A*, right; Le Masson et al., 2014). *In silico* modeling has revealed that the outcome of mitochondrial dysfunction and diminished pump activity is a "deadly loop" comprised of a rapidly burgeoning demand for ATP that remains unmet, and Ca^{2+} dyshomeostasis (Le Masson et al., 2014). Since our findings of diminished Ca^{2+} extrusion in neurons expressing *vapb*^{P58S} (Fig. 5*G*) aligns with the notion of Ca^{2+} dyshomeostasis, we asked whether the expression of *vapb*^{P58S} compromises mitochondrial ATP production, which in principle, could preclude a suitable response to depolarization and [Ca^{2+}] elevation.

Given that mitochondrial Ca^{2+} uptake, needed for energizing those organelles and stimulating TCA dehydrogenases, is disrupted in *vapb*^{P58S}-expressing neurons, it stood to reason that "on-demand" ATP production would be attenuated in these neurons (Duchen, 1992; McCormack and Denton, 1993; Dumollard

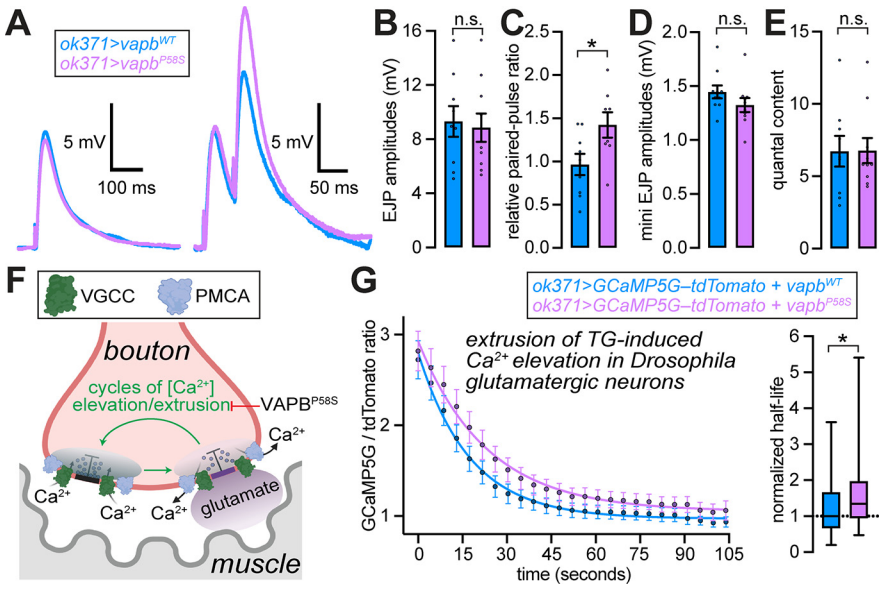

Figure 5. Expression of *vapb*^{P58S} results in delayed extrusion of cytosolic Ca^{2+}. ***A***, Representative EJP (left) and paired-pulse EJP (right) traces recorded from larval NMJs isolated from animals expressing *vapb*^{WT} (blue trace) or *vapb*^{P58S} (magenta trace) in motor neurons using *ok731-GAL4*. ***B***, Bar graph showing quantification of the EJP amplitudes from the data shown in ***A***. Values represent mean ± SEM; n.s., not significant, paired *t* tests. Dots represent values from distinct NMJs. ***C***, Bar graph showing quantification of the paired-pulse ratio (fractional change in the amplitude of the second EJP to that of the first EJP when the two stimulatory pulses were applied 50 ms apart) of the data shown in ***A***. Values represent mean ± SEM; $*p < 0.05$, *t* test. Dots represent values from distinct NMJs. ***D***, Bar graph showing quantification of the mini EJP amplitudes. Values represent mean ± SEM; n.s., not significant, paired *t* tests. Dots represent values from distinct NMJs. ***E***, Bar graph showing quantification of quantal content (ratio of amplitudes of EJP and mini EJP). Values represent mean ± SEM; n.s., not significant, paired *t* tests. Dots represent values from distinct NMJs. ***F***, Model showing that the rates of $[Ca^{2+}]$ elevation and extrusion are necessary for maintaining the fidelity of synaptic transmission. Paired-pulse facilitation without a change in the amplitude of the first pulse, as seen in ***A***, could be explained by VAPB^{P58S} decreasing the rates of Ca^{2+} extrusion. Image was created with BioRender. ***G***, Left, Traces showing the decay of GCaMP5G/tdTomato ratio after TG-induced cytosolic $[Ca^{2+}]$ elevations in motor neurons dissociated from animals of the indicated genotypes. Values were fit to a first order exponential function. Values represent mean ± SEM of traces from >50 neurons of each genotype. Right, Box plots showing quantification of half-lives of decay of the signals in individual neurons of the indicated genotypes; $*p < 0.05$, Mann–Whitney test. Refer to Table 5 for statistical information.

et al., 2004; Cárdenas et al., 2010; Ding et al., 2018; Wong et al., 2021). To test this idea, we monitored the cytosolic [ATP]/[ADP] ratio in larval motor neurons using the genetically-encoded sensor, PercevalHR (Tantama et al., 2013; Wong et al., 2021). In neurons coexpressing *vapb*^{WT}, depolarization by the application of high $[K^+]$ (52 mM) led to a transient decrease in the PercevalHR ratio (i.e., [ATP]/[ADP] ratio), whereas the ratio remained unchanged in neurons not challenged with high $[K^+]$ (Fig. 6*B*). In *vapb*^{P58S}-expressing neurons, however, high $[K^+]$ led to a more sustained decline in the PercevalHR ratio (Fig. 6*B*, see below for quantification of cumulative decline).

Since prior reports have indicated that *vapb*^{P58S} exerts its effects in fly neurons via a dominant-negative mode of action (Ratnaparkhi et al., 2008), we asked whether a reduction in *vapb* expression would result in a similar defect in sustaining the [ATP]/[ADP] ratio on depolarization. We obtained a transgenic line for *vapb* knock-down, *vapb*^{RNAi}, which significantly reduced *vapb* mRNA levels (Fig. 6*C*). Upon coexpression with PercevalHR in motor neurons, *vapb*^{RNAi} led to a sustained decrease in the [ATP]/[ADP] ratio in response to depolarization with high $[K^+]$ (Fig. 6*D*). Comparison of the cumulative change in the PercevalHR ratio per unit time revealed that neurons expressing *vapb*^{P58S} or *vapb*^{RNAi} exhibited a significantly greater cumulative decrease in PercevalHR ratio in response to high $[K^+]$ than did neurons expressing *vapb*^{WT} (Fig. 6*E*). In contrast, the cumulative changes in *vapb*^{P58S} or *vapb*^{RNAi} were not statistically significant (Fig. 6*E*). These data indicate that neurons expressing *vapb*^{P58S} or *vapb*^{RNAi} were less capable of responding to the ATP burden of depolarization than were neurons with expressing *vapb*^{WT}. Recovery of the PercevalHR ratio during a 30-s window after application of high $[K^+]$ (Fig. 6*B*,*D*, green lines), was significantly greater in neurons overexpressing *vapb*^{WT} than they were in neurons expressing *vapb*^{P58S} or *vapb*^{RNAi} (Fig. 6*F*). These data show that the rate at which the [ATP]/[ADP] ratio recovers after depolarization is diminished in neurons expressing *vapb*^{P58S} or *vapb*^{RNAi}. Finally, we asked whether knock-down of *vapb* also delays the extrusion of cytosolic Ca^{2+} as we had observed in neurons expressing *vapb*^{P58S}. Relative to neurons not expressing the RNAi transgene, those expressing *vapb*^{RNAi} exhibited delayed recovery from TG-induced $[Ca^{2+}]$ elevation (Fig. 6*G*). Together, these data indicate that either the knock-down of *vapb* or the expression of *vapb*^{P58S} in *Drosophila* motor neurons compromised the neurons' response to the bioenergetic burden of depolarization, and delayed the rates at which they extrude Ca^{2+}. These conclusions agree with the predictions made by *in silico* modeling of ALS neurons (Fig. 6*A*; Le Masson et al., 2014).

Next, we examined the role of OXPHOS in the observed bioenergetic alterations. We found that application of the ATP synthase inhibitor, oligoA, led to the expected decrease of the [ATP]/[ADP] ratio in neurons expressing *vapb*^{WT}, *vapb*^{P58S}, or *vapb*^{RNAi}, regardless of whether the neurons were exposed to normal or high $[K^+]$ (Fig. 7*A*,*B*). The cumulative decreases in ratio after inhibition of OXPHOS were comparable in the *vapb*^{WT} and *vapb*^{P58S} neurons (Fig. 7*A*,*B*). These data imply that on cessation of ATP production, the [ATP]/[ADP] ratio comes to rest at similar values in neurons expressing either *vapb*^{WT} or *vapb*^{P58S}. These data argue that neuronal [ADP] is not significantly altered in neurons of the two genotypes. In agreement, the cumulative decrease in [ATP]/[ADP] ratio was reduced in depolarized neurons because the burden of depolarization had lowered the [ATP]/[ADP] ratio, even before the application of oligoA. Taken together, our data indicate that the greater cumulative decline in the [ATP]/[ADP] ratio in depolarized *vapb*^{P58S} neurons, as evident from Figure 6*E*, reflects the diminished rates of ATP synthesis rather than changes in substrate (i.e., ADP) availability. In neurons expressing *vapb*^{RNAi1}, however, oligoA-induced reduction in the [ATP]/[ADP] ratio was significantly higher than that in the other two genotypes, both at normal and high $[K^+]$ (Fig. 7*A*,*B*). These data argue in favor of higher [ADP] in those neurons, which is likely a compensatory response to *vapb* knock-down.

Loss of synaptic transmission during high-frequency stimulation in *vapb*^{P58S}-expressing motor neurons

Many *vapb*^{P58S} phenotypes we describe in this study, including elevated $[Ca^{2+}]$ and limited [ATP], are also observed in *drp1*-

Table 5. Statistical information for the data shown in Figure 5

Figure 5*B*

Genotype	Normally distributed?	Values	Number of animals
d42>vapb^{WT}	Yes	9.3 ± 1.1	5 (*n* = 10 NMJs)
d42>vapb^{P58S}	Yes	8.9 ± 1.0	5 (*n* = 10 NMJs)

Comparison between	Test used	*P*-value	Test statistics
d42>vapb^{WT} *d42>vapb*^{P58S}	*t* test	0.77	*t* = 0.2961, df = 16.68

Figure 5*C*

Genotype	Normally distributed?	Values	Number of animals
d42>vapb^{WT}	Yes	0.97 ± 0.12	5 (*n* = 10 NMJs)
d42>vapb^{P58S}	Yes	1.42 ± 0.15	5 (*n* = 10 NMJs)

Comparison between	Test used	*P*-value	Test statistics
d42>vapb^{WT} *d42>vapb*^{P58S}	*t* test	0.03	*t* = 2.388, df = 14.14

Figure 5*D*

Genotype	Normally distributed?	Values	Number of animals
d42>vapb^{WT}	Yes	1.44 ± 0.06	5 (*n* = 10 NMJs)
d42>vapb^{P58S}	Yes	1.32 ± 0.07	5 (*n* = 10 NMJs)

Comparison between	Test used	*P*-value	Test statistics
d42>vapb^{WT} *d42>vapb*^{P58S}	*t* test	0.19	*t* = 1.372, df = 17.83

Figure 5*E*

Genotype	Normally distributed?	Values	Number of animals
d42>vapb^{WT}	Yes	6.73 ± 1.1	5 (*n* = 10 NMJs)
d42>vapb^{P58S}	No	6.78 ± 0.9	5 (*n* = 10 NMJs)

Comparison between	Test used	*P*-value	Test statistics
d42>vapb^{WT} *d42>vapb*^{P58S}	Mann–Whitney	0.9	*U* = 43

Figure 5*G*

Genotype	Normally distributed?	Values	
d42>vapb^{WT}	No	median = 1	
d42>vapb^{P58S}	No	median = 1.6	
Comparison between	Test used	*P*-value	Test statistics
d42>vapb^{WT} *d42>vapb*^{P58S}	Mann–Whitney	0.04	*U* = 726

deficient animals (Verstreken et al., 2005). Since the paucity of ATP in *drp1* mutant NMJs precludes the maintenance of synaptic transmission during high-frequency stimulation (Verstreken et al., 2005), we asked whether the shortage of ATP in *vapb*^{P58S} motor neurons would result in similar rundown of SV release. Although stimulation of the *vapb*^{P58S} NMJs at 10 Hz led to EJP amplitudes that initially plateaued at values that were ~35% higher than baseline, those values transitioned to periods of sustained decay after ~5 min of high-frequency stimulation (Fig. 7*C*, left, traces with filled circles, green arrow indicates onset of decay). EJP amplitudes in 100% of the traces recorded from *vapb*^{P58S} animals stimulated at 10 Hz exhibited sustained periods of decay after initial, transient elevations. We reasoned that superimposed on the liminal increase in EJP amplitudes were the rundowns of SV release, which become apparent after ~5 min of high-frequency stimulation. We extracted the rundown components from the traces using the rate-constants of the decay (Fig. 7*C*, left, traces with filled squares). Over the 10 min duration of the high-frequency stimulation, calculated rundowns in *vapb*^{P58S} NMJs dropped significantly lower than baseline (Fig. 7*C*, left). The decay phase of high-frequency traces recorded from *vapb*^{WT} NMJs was relatively less-pronounced (Fig. 7*C*, right), with only 40% of the traces exhibiting sustained periods of declining EJP values. Calculated rundown in *vapb*^{WT} NMJs was not significantly lower than baseline (Fig. 7*C*, right). Therefore, high-frequency stimulation leads to a greater loss of synaptic transmission in *vapb*^{P58S}-expressing motor neurons. In agreement, calculated rundowns in *vapb*^{P58S} were predicted to plateau at 3.82 mV [95% confidence interval (CI), 3.69–3.94, $p < 0.0001$], whereas rundowns were predicted to plateau at 11.96 mV (95% CI, 11.81–12.11, $p < 0.0001$) in *vapb*^{WT}.

Bioenergetic dysfunction and attendant changes in SV cycling at the *drp1* mutant NMJs stem from the absence of local mitochondria because of defects in mitochondrial trafficking to the axon termini (Verstreken et al., 2005). In contrast, coexpression of the mitochondrial marker, *mCherry-mito-OMM* (Vagnoni and Bullock, 2016), with the *vapb* variants belied putative defects in the availability of mitochondria at the NMJ (Fig. 7*D*,*E*). Mitochondria in the *vapb*^{P58S}-expressing neurons did, however, exhibit subtle morphologic changes, slight yet significant increases in the relative volume and surface-area of each mitochondrion at the termini (Fig. 7*F*,*G*). Mitochondrial aspect ratio (i.e., the volume/surface area ratio of each mitochondrion) was ~2% lower in *vapb*^{P58S} NMJs (Fig. 7*H*), which argues against meaningful changes in fission–fusion dynamics. Collectively, our data argue against changes in mitochondrial trafficking or dynamics as the underlying cause for rundown of synaptic transmission in *vapb*^{P58S} NMJs.

Discussion

Our findings explain the characteristic changes to NMJ morphology observed in animals that harbor *vapb* deletions or express an ALS-causing variant of the gene (*vapb*^{P58S}; Pennetta et al., 2002; Chai et al., 2008; Ratnaparkhi et al., 2008). While it was known that the reduction in NMJ bouton number and increase in bouton size stem from diminished stability of presynaptic microtubules (Pennetta et al., 2002; Chai et al., 2008; Ratnaparkhi et al., 2008), the molecular underpinnings of these cytoskeletal changes had remained unclear. Our finding that nocodazole decreased the number of presynaptic microtubule loops in neurons expressing *vapb*^{WT}, but not in neurons expressing *vapb*^{P58S}, argues in favor of microtubule-depolymerization being constitutively elevated in the latter. The additional finding that the morphologic defects in *vapb*^{P58S} NMJs were attenuated by inhibition of CaMKII implicates aberrant CaMKII activation in the observed NMJ phenotypes. These conclusions agree with prior reports of CaMKII regulating microtubule stability by phosphorylating microtubule-associated proteins (Baratier et al., 2006; McVicker et al., 2015; Oka et al., 2017).

We speculate that the MAP1b homolog, Futsch (Hummel et al., 2000; Roos et al., 2000), is the relevant CaMKII target in this context. Previous studies have shown that hyperphosphorylation of Futsch, which provokes microtubule destabilization, results in the loss of Futsch-loops within NMJ boutons (Gögel et al., 2006; Viquez et al., 2006; Wong et al., 2014). The potential involvement of Futsch also agrees with prior reports of reduced Futsch abundance at the NMJ in a fly model of TDP-43-induced proteinopathy, primarily because of diminished translation of *futsch* mRNA (Coyne et al., 2014). Therefore, microtubule destabilization with the underlying involvement of Futsch could be a common occurrence in *Drosophila* models of ALS (Pennetta et al., 2002; Ratnaparkhi et al., 2008; Coyne et al., 2014). Interestingly,

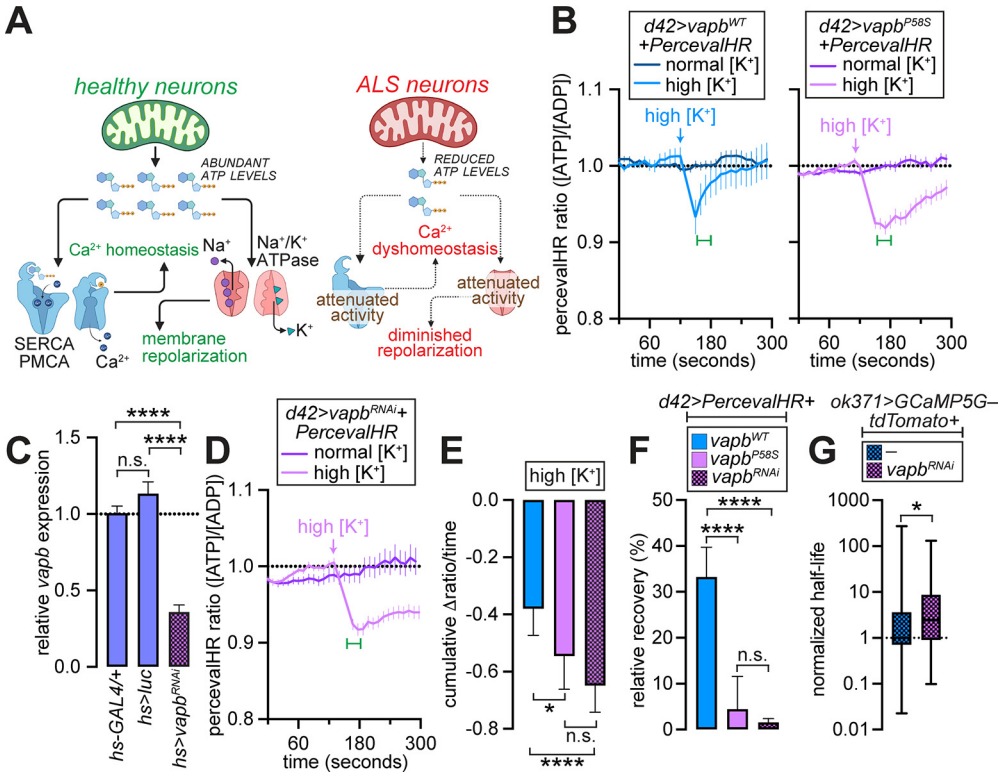

Figure 6. Response to ATP burden of depolarization in motor neurons depends on the presence of functional *vapb*. ***A***, Model adapted from Le Masson et al. (2014) showing the role for neuronal ATP in mediating ionic homeostasis. In healthy neurons, ATP derived from mitochondrial oxidative phosphorylation (OXPHOS) powers Ca^{2+} ATPases, such as SERCA and PMCA, to maintain Ca^{2+} homeostasis, and the Na^+/K^+ ATPase, which is needed for setting the resting membrane potential and for repolarization of the membrane potential after bouts of depolarization. In ALS neurons, a decrease in mitochondrial ATP production would attenuate the activities of Ca^{2+}- and Na^+/K^+-ATPases. This would be predicted to set in motion a self-reinforcing "deadly loop" comprised of continuously increasing ATP consumption coupled with diminished ATP availability, Ca^{2+} dyshomeostasis, and the eventual loss of membrane potential. Image was created with BioRender. ***B***, ***D***, Representative traces showing normalized PercevalHR ratios in *Drosophila* motor neurons coexpressing the indicated transgenes. Values represent mean ± SEM of traces from >20 neurons of each genotype. Arrows indicate treatments. ***C***, Bar graph showing relative *vapb* expression in animals of the indicated genotypes. Values were normalized to the mean in *hs-GAL4/+*, and represent mean ± SEM; $^{****}p < 0.0001$; n.s., not significant, *t* tests with Bonferroni correction. ***E***, Bar graph showing the cumulative change in the PercevalHR ratio per unit time in neurons dissociated from animals of the indicated genotypes. Values < 0 denote a net decrease in the PercevalHR ratio (i.e., [ATP]/[ADP] ratio) after application of high $[K^+]$. Values represent median ± 95% CIs; $^{*}p < 0.05$, $^{****}p < 0.0001$; n.s., not significant, Mann–Whitney tests with Bonferroni correction. ***F***, Bar graph showing the recovery of PercevalHR ratio during a 30-s window depicted by the green lines in the traces shown in ***B*** and ***D***. Values represent median ± 95% CIs; $^{****}p < 0.0001$; n.s., not significant, Mann–Whitney tests with Bonferroni correction. ***G***, Box plots showing quantification of half-lives of decay of the GCaMP5G/tdTomato ratio after TG-induced cytosolic $[Ca^{2+}]$ elevations in motor neurons dissociated from animals of the indicated genotypes; $^{***}p < 0.001$, Mann–Whitney test. Refer to Table 6 for statistical information.

expression of a gain-of-function variant of *vapb* results in the opposite phenotype, increased number of synaptic boutons and Futsch loops (Sanhueza et al., 2014). Given the likelihood that $VAPB^{P58S}$ acts via a dominant-negative mode of action (Ratnaparkhi et al., 2008), there appears to be a direct correlation between the functionality and dosage of VAPB, Futsch-dependent microtubule stability, and bouton number at the larval NMJ (Pennetta et al., 2002; Sanhueza et al., 2014).

Ectopic expression of an overactive TRPV4 channel variant that elevates intracellular $[Ca^{2+}]$ and induces neuropathology via CaMKII hyperactivation (Woolums et al., 2020) sets a precedent for the notion that aberrant CaMKII activation in motor neurons implies higher cytosolic $[Ca^{2+}]$. Blocking the sources of presynaptic Ca^{2+} elevation, then, would be expected to restore Ca^{2+} homeostasis, and thereby, ameliorate the consequences of CaMKII hyperactivation. Indeed, reduced expression of ER Ca^{2+} release channels in *Drosophila* neurons counteracts the phenotypes stemming from activating mutations in a voltage-gated Ca^{2+} channel (Brusich et al., 2018). We found that lowering the abundance of any one of the three presynaptic ER Ca^{2+} release channels, Iav, RyR, and IP_3R, restored bouton morphology and number in neurons expressing $vapb^{P58S}$. These data also point to the existence of a biphasic, bell-shaped relationship between presynaptic $[Ca^{2+}]$ and NMJ morphology, whereby either a supraphysiological increase or decrease in $[Ca^{2+}]$ elicits morphologically indistinguishable changes at the NMJ.

Do the effects of ER Ca^{2+} channel knock-down or $CKII^{ala}$ expression on NMJ development in larvae expressing $vapb^{P58S}$ correlate with functional alterations in locomotion?

To answer this question, we first asked whether expression of $vapb^{P58S}$ in motor neurons leads to alterations in larval locomotion. We found that crawling velocity in an open field was significantly reduced in larvae expressing $vapb^{P58S}$ relative to those expressing $vapb^{WT}$. Concomitant knock-down of the gene encoding IP_3R or expression of $CKII^{ala}$ prevented this decrease in the velocity of peristalsis in $vapb^{P58S}$-expressing larvae. Expression of $vapb^{P58S}$ in motor neurons also leads to premature lethality in adult animals (Wong et al., 2021). In contrast to its restorative effects on NMJ development and larval locomotion, $CKII^{ala}$ had no effect on the abbreviated lifespan observed in adult flies expressing $vapb^{P58S}$ in motor neurons. Therefore, the developmental and longevity phenotypes stem from partially

Table 6. Statistical information for the data shown in Figure 6

Figure 6C

Genotype	Normally distributed?	Values
hs-GAL4/+	Yes	1.0 ± 0.05
hs>luc	Yes	1.1 ± 0.08
hs>vapb^{P58S}	Yes	0.4 ± 0.05

Comparison between	Test used	*P*-value	Test statistics
hs-GAL4/+ *hs>luc*	*t* test followed by Bonferroni correction	0.6	$t = 1.414$, df = 8.165
hs-GAL4/+ *hs>vapb^{P58S}*	*t* test followed by Bonferroni correction	<0.0001	$t = 9.808$, df = 9.999
hs-GAL4/+ *hs>luc*	*t* test followed by Bonferroni correction	<0.0001	$t = 8.539$, df = 8.209

Figure 6E

Genotype	Normally distributed?	Values (median, lower CI, upper CI)
d42>PercevalHR+vapb^{WT}	No	(−0.38, −0.47, −0.25)
d42>PercevalHR+vapb^{P58S}	No	(−0.55, −0.66, −0.42)
d42>PercevalHR+vapb^{RNAi}	No	(−0.65, −0.74, −0.50)

Comparison between	Test used	*P*-value	Test statistics
d42>PercevalHR+vapb^{WT} *d42>PercevalHR+vapb^{P58S}*	Mann–Whitney followed by Bonferroni correction	0.01	$U = 44192$
d42>PercevalHR+vapb^{P58S} *d42>PercevalHR+vapb^{RNAi}*	Mann–Whitney followed by Bonferroni correction	<0.0001	$U = 39586$
d42>PercevalHR+vapb^{WT} *d42>PercevalHR+vapb^{RNAi}*	Mann–Whitney followed by Bonferroni correction	0.45	$U = 35319$

Figure 6F

Genotype	Normally distributed?	Values (median, lower CI, upper CI)
d42>PercevalHR+vapb^{WT}	No	(33.24, 26.88, 39.73)
d42>PercevalHR+vapb^{P58S}	No	(4.47, 0.33, 11.59)
d42>PercevalHR+vapb^{RNAi}	No	(1.55, 1.06, 2.38)

Comparison between	Test used	*P*-value	Test statistics
d42>PercevalHR+vapb^{WT} *d42>PercevalHR+vapb^{P58S}*	Mann–Whitney followed by Bonferroni correction	<0.0001	$U = 15458$
d42>PercevalHR+vapb^{P58S} *d42>PercevalHR+vapb^{RNAi}*	Mann–Whitney followed by Bonferroni correction	0.21	$U = 24263$
d42>PercevalHR+vapb^{WT} *d42>PercevalHR+vapb^{RNAi}*	Mann–Whitney followed by Bonferroni correction	<0.0001	$U = 13935$

Figure 6G

Genotype	Normally distributed?	Values (median, lower CI, upper CI)
ok731>GCaMP5G-tdTomato	No	Median = 1
ok731>GCaMP5G-tdTomato+vapb^{RNAi}	No	Median = 2.5

Comparison between	Test used	*P*-value	Test statistics
ok731>GCaMP5G-tdTomato *ok731>GCaMP5G-tdTomato+vapb^{RNAi}*	Mann–Whitney	0.01	$U = 1410$

overlapping, yet distinct, molecular pathways. While the NMJ and larval motor phenotypes were suppressed by concomitant reductions in the abundance of Iav and RyR, or by the expression of the CaMKII inhibitory peptide, none of these manipulations influenced the effects of VAPB^{P58S} on adult lifespan. Only with the knock-down of the gene encoding IP_3Rs do we observe suppression of NMJ development phenotypes, larval locomotion, and adult lethality, though the former two likely involve CMKII attenuation while the latter, as we showed previously (Wong et al., 2021), stems from mitigation of endolysosomal [Ca^{2+}] overload.

Given that the NMJ phenotypes in neurons expressing *vapb^{P58S}* were suppressed by the loss of ER Ca^{2+} channels, which are needed for maintaining presynaptic resting [Ca^{2+}] (Wong et al., 2014), we asked whether VAPB^{P58S} was triggering an increase in resting [Ca^{2+}]. Higher presynaptic resting [Ca^{2+}] augments the probability of SV release resulting in increased amplitudes of evoked postsynaptic potentials that is accompanied by paired-pulse depression (Wong et al., 2014). In agreement with prior reports (Chai et al., 2008), we found that expression of *vapb^{P58S}* induced neither a change in the amplitude of evoked potentials nor the appearance of paired-pulse depression. Rather, *vapb^{P58S}* NMJs exhibited paired-pulse facilitation, which in combination with the absence of changes in the amplitude of evoked potentials, was consistent with poststimulus accumulation of residual Ca^{2+} because of delayed extrusion of presynaptic Ca^{2+}. Indeed, direct examination of cytosolic [Ca^{2+}] using GCaMP5G-tdTomato revealed significantly delayed Ca^{2+} extrusion in *vapb^{P58S}*-expressing motor neurons. These data indicate that the aberrant activation of CaMKII in *vapb^{P58S}*-expressing neurons arose from the accumulation of residual Ca^{2+} because of delayed extrusion.

What could explain the defects in Ca^{2+} extrusion in neurons expressing *vapb^{P58S}*?

The plasma membrane-resident Ca^{2+} ATPase, PMCA, has been shown to play a major role in the extrusion of presynaptic Ca^{2+} in *Drosophila* motor neurons (Ivannikov and Macleod, 2013; Rossano et al., 2013). Given the bioenergetic burden of powering PMCA, we reasoned that a shortage of ATP could underlie the Ca^{2+} dyshomeostasis observed in *vapb^{P58S}*-expressing neurons.

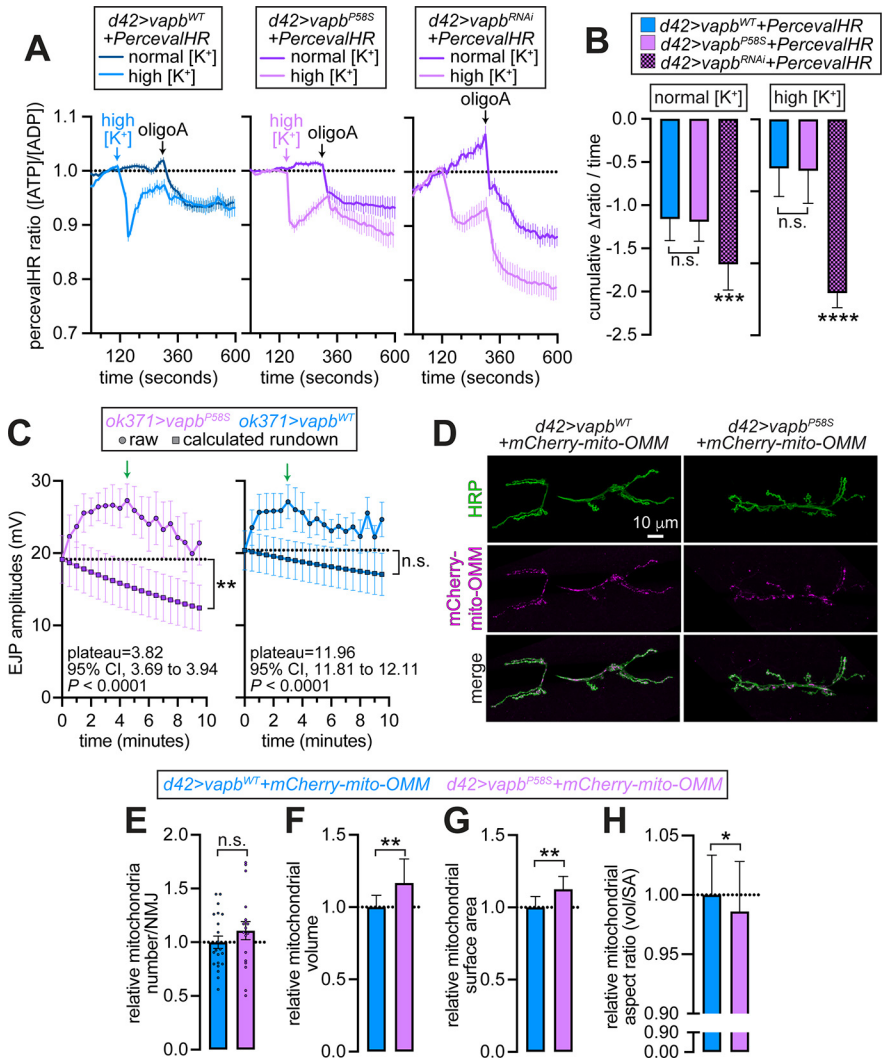

Figure 7. oligoA-induced changes in the [ATP]/[ADP] ratio, and effects of high-frequency stimulation in neurons expressing *vapb* variants. ***A***, Traces showing PercevalHR ratio after application of oligoA in neurons dissociated from animals of the indicated genotypes. Values represent mean ± SEM of traces from >20 neurons of each genotype. Arrows indicate treatments. ***B***, Bar graph showing the cumulative change in the PercevalHR ratio per unit time in neurons dissociated from animals of the indicated genotypes. Values represent median ± 95% CIs; ***$p < 0.001$, ****$p < 0.0001$; n.s., not significant, Kruskal–Wallis and Mann–Whitney tests. ***C***, Traces showing EJP amplitudes recorded from NMJs of animals of the indicated genotypes stimulated at 10 Hz for 10 min. Traces connecting filled circles represent raw values that were determined experimentally, and the traces connecting filled-squares represent calculated rundowns fit to first order exponential decay. Green arrows indicate the onset of decay. All values represent mean ± SEM of EJP values recorded from five NMJ preparations of each genotype; **$p < 0.01$; n.s., not significant, paired *t* tests. ***D***, Representative confocal images of larval NMJs dissected from animals of the genotypes indicated on the top and stained with antibodies against HRP (green). Mitochondria were labeled by mCherry-mito-OMM (magenta). Scale bar shown in top left image applies to all the images in the panel. ***E–H***, Bar graphs showing quantification of the parameters of mitochondrial morphology in animals of the indicated genotypes. Values were normalized to the control mean (***E***) or to the control median (***F–H***). Values represent mean ± SEM (***E***) or median ± 95% CIs (***F–H***). In ***E***, n.s., not significant, *t* test, and circles represent values from distinct NMJs. In ***F–H***, *$p < 0.05$, **$p < 0.01$; Mann–Whitney tests. Refer to Table 7 for statistical information.

In support of this model, mutated VAPB has been shown to disrupt interorganellar transfer of Ca^{2+} from the ER to mitochondria in both mammalian cells and *Drosophila* neurons (De Vos et al., 2012; Stoica et al., 2016; Gomez-Suaga et al., 2017; Smith et al., 2017; Xu et al., 2020; Wong et al., 2021). Given the role of matrix $[Ca^{2+}]$ in ATP production (Duchen, 1992; McCormack and Denton, 1993; Dumollard et al., 2004; Cárdenas et al., 2010; Ding et al., 2018), we asked whether expression of $vapb^{P58S}$ compromised mitochondrial ATP production. By examining the [ATP]/[ADP] ratio in live neurons, we found that the bioenergetic response to depolarization was relatively stunted in $vapb^{P58S}$-expressing neurons. The cumulative decrease in [ATP]/[ADP] ratio in depolarized $vapb^{P58S}$-expressing neurons was greater than that in neurons expressing $vapb^{WT}$. Eventual recovery of the [ATP]/[ADP] ratio in depolarized neurons was faster if they overexpressed $vapb^{WT}$, which points to the sufficiency of *vapb* in sculpting the kinetics of neurons' response to the bioenergetic burden of depolarization. Consistent with $VAPB^{P58S}$ having a dominant negative mode of action (Ratnaparkhi et al., 2008), neurons expressing an RNAi line against *vapb* also exhibit larger cumulative decrease in the [ATP]/[ADP] ratio, and delayed extrusion of cytosolic Ca^{2+}.

Upon cessation of OXPHOS by application of the ATP synthase inhibitor, oligoA, we found that cumulative decreases in the [ATP]/[ADP] ratio were comparable in neurons expression either *vapb* variant. Strictly speaking, the levels at which the cytosolic [ATP]/[ADP] ratio settles following application of oligoA, are functions of two parameters: (1) levels of a pool of ATP that is either not available for hydrolysis or is generated from a source other than OXPHOS; and (2) free [ADP]. Absence of evidence supporting the presence of nonhydrolyzable depots of ATP in the cytosol of neuronal cell bodies, however, argues that the cumulative decrease in the [ATP]/[ADP] reflects the abundance of ADP available for ATP synthesis. By extension, the sluggish response to bioenergetic demands of depolarization in $vapb^{P58S}$ neurons does not stem from diminished substrate availability. Rather, the rates of ATP synthesis from ADP are likely lower in those neurons, although elevated rates of ATP hydrolysis could also be contributing to the phenotype. Indeed, *in silico* modeling has predicted that mitochondrial dysfunction in ALS neurons is sufficient to induce a toxic self-reinforcing loop of increased ATP consumption and a progressive decrease in the availability of ATP (Le Masson et al., 2014). In neurons expressing the RNAi line against *vapb*, oligoA-induced cumulative decrease in [ATP]/[ADP] ratio was significantly greater than in the other genotypes. These data argue in favor of basally higher net [ADP] on *vapb* knock-down, which could be a compensatory response to sustained defects in ATP production. The fact that these neurons were still unable to meet the bioenergetic demands of depolarization speaks to profound defects in activity-dependent ATP synthesis in neurons with lower *vapb* expression. The apparent absence of compensation in neurons expressing $vapb^{P58S}$ could imply a role for *vapb*

Table 7. Statistical information for the data shown in Figure 7

Figure 7*B*

Genotype	Normally distributed?	Values (median, lower CI, upper CI)
d42>PercevalHR+vapb^{WT} norm K	No	(−1.16, −1.41, −1.01)
d42>PercevalHR+vapb^{P58S} norm K	No	(−1.19, −1.42, −0.78)
d42>PercevalHR+vapb^{RNAi} norm K	No	(−2.08, −1.98, −1.48)
d42>PercevalHR+vapb^{WT} high K	No	(−0.34, −0.54, −0.23)
d42>PercevalHR+vapb^{P58S} high K	No	(−0.36, −0.58, −0.28)
d42>PercevalHR+vapb^{RNAi} high K	No	(−1.21, −1.31, −0.99)

Comparison between	Test used	*P*-value	Test statistics
d42>PercevalHR+vapb^{WT} norm K *d42>PercevalHR+vapb^{P58S}* norm K	Mann–Whitney followed by Bonferroni correction	1	$U = 2637$
d42>PercevalHR+vapb^{WT} norm K *d42>PercevalHR+vapb^{P58S}* norm K *d42>PercevalHR+vapb^{RNAi}* norm K	Kruskal–Wallis	0.0004	Kruskal–Wallis statistic = 15.58
d42>PercevalHR+vapb^{WT} high K *d42>PercevalHR+vapb^{P58S}* high K	Mann–Whitney followed by Bonferroni correction	0.9	$U = 1706$
d42>PercevalHR+vapb^{WT} norm K *d42>PercevalHR+vapb^{P58S}* norm K *d42>PercevalHR+vapb^{RNAi}* norm K	Kruskal–Wallis	<0.0001	Kruskal–Wallis statistic = 65.55

Figure 7*C*

Comparison between	Test used	*P*-value	Test statistics
ok371>vapb^{WT}	paired *t* test	0.18	$t = 1.632$, df = 4
ok371>vapb^{P58S}	paired *t* test	0.001	$t = 8.347$, df = 4

Figure 7*E*

Genotype	Normally distributed?	Values	Number of animals
d42>mCherry-mito-OMM+vapb^{WT}	Yes	1.0 ± 0.06	11 ($n = 21$ NMJs)
d42>mCherry-mito-OMM+vapb^{P58S}	Yes	1.1 ± 0.08	9 ($n = 18$ NMJs)

Comparison between	Test used	*P*-value	Test statistics
d42>mCherry-mito-OMM+vapb^{WT} d42>mCherry-mito-OMM+vapb^{P58S}	*t* test	0.3	$t = 1.058$, df = 30.65

Figure 7*F*

Genotype	Normally distributed?	Values (median, lower CI, upper CI)	Number of animals
d42>mCherry-mito-OMM+vapb^{WT}	No	(1.0, 0.92, 1.1)	11 ($n = 21$ NMJs)
d42>mCherry-mito-OMM+vapb^{P58S}	No	(1.2, 1.1, 1.3)	9 ($n = 18$ NMJs)

Comparison between	Test used	*P*-value	Test statistics
d42>mCherry-mito-OMM+vapb^{WT} d42>mCherry-mito-OMM+vapb^{P58S}	Mann–Whitney	0.0025	$U = 2{,}042{,}530$

Figure 7*G*

Genotype	Normally distributed?	Values (median, lower CI, upper CI)	Number of animals
d42>mCherry-mito-OMM+vapb^{WT}	No	(1.0, 0.94, 1.1)	11 ($n = 21$ NMJs)
d42>mCherry-mito-OMM+vapb^{P58S}	No	(1.12, 1.1, 1.2)	9 ($n = 18$ NMJs)

Comparison between	Test used	*P*-value	Test statistics
d42>mCherry-mito-OMM+vapb^{WT} d42>mCherry-mito-OMM+vapb^{P58S}	Mann–Whitney	0.0071	$U = 2{,}055{,}518$

Figure 7*H*

Genotype	Normally distributed?	Values (median, lower CI, upper CI)	Number of animals
d42>mCherry-mito-OMM+vapb^{WT}	No	(1.0, 0.97, 1.03)	11 ($n = 21$ NMJs)
d42>mCherry-mito-OMM+vapb^{P58S}	No	(0.98, 0.92, 1.03)	9 ($n = 18$ NMJs)

Comparison between	Test used	*P*-value	Test statistics
d42>mCherry-mito-OMM+vapb^{WT} d42>mCherry-mito-OMM+vapb^{P58S}	Mann–Whitney	0.01	$U = 2{,}060{,}657$

dosage in initiating the compensatory response. Nevertheless, the paucity of [ATP] in *vapb^{P58S}*-expressing neurons during periods of depolarization (i.e., neuronal activity), is consistent with diminished Ca^{2+} extrusion, which in-turn could provoke the hyperactivation of CaMKII and attendant changes in NMJ morphology.

Maintenance of synaptic transmission at *Drosophila* larval NMJs during periods of high-frequency stimulation depends on

a steady supply of ATP. A local shortage of ATP, for instance, because of an absence of presynaptic mitochondria in *drp1* mutants, results in rundown of SV release during high-frequency stimulation (Verstreken et al., 2005). These rundowns occur because of the inability of the synapses to meet the energy demands of SV cycling, and diminished recruitment of the reserve pool of SVs that are otherwise mobilized to replace the rapid depletion of the readily-releasable pool of vesicles (Verstreken et al., 2005). In either the $vapb^{WT}$-expressing or $vapb^{P58S}$-expressing NMJs, high frequency stimulation led to initial elevation of synaptic transmission. Superimposed over these liminal elevations were rundowns that became obvious after ~5 min of stimulation, and were significantly greater in $vapb^{P58S}$-expressing neurons. These data agree with enhanced rundown of SV release in motor neurons expressing $vapb^{P58S}$. The magnitude of this phenotype, however, was smaller than that observed in the *drp1* mutants (Verstreken et al., 2005). This discrepancy is explained by the absence of presynaptic mitochondria in *drp1* mutant neurons (Verstreken et al., 2005), while we observed no significant changes in the number of presynaptic mitochondria in $vapb^{P58S}$. The relative severity of rundown at *drp1* mutant NMJs is likely because of constitutively lower [ATP] in those mutants (Verstreken et al., 2005), whereas shortage of ATP in $vapb^{P58S}$-expressing neurons is contingent on depolarization.

References

Anagnostou G, Akbar MT, Paul P, Angelinetta C, Steiner TJ, de Belleroche J (2010) Vesicle associated membrane protein B (VAPB) is decreased in ALS spinal cord. Neurobiol Aging 31:969–985.

Baratier J, Peris L, Brocard J, Gory-Fauré S, Dufour F, Bosc C, Fourest-Lieuvin A, Blanchoin L, Salin P, Job D, Andrieux A (2006) Phosphorylation of microtubule-associated protein STOP by calmodulin kinase II. J Biol Chem 281:19561–19569.

Bloomquist BT, Shortridge RD, Schneuwly S, Perdew M, Montell C, Steller H, Rubin G, Pak WL (1988) Isolation of a putative phospholipase C gene of *Drosophila*, norpA, and its role in phototransduction. Cell 54:723–733.

Boczonadi V, Meyer K, Gonczarowska-Jorge H, Griffin H, Roos A, Bartsakoulia M, Bansagi B, Ricci G, Palinkas F, Zahedi RP, Bruni F, Kaspar B, Lochmüller H, Boycott KM, Müller JS, Horvath R (2018) Mutations in glycyl-tRNA-synthetase impair mitochondrial metabolism in neurons. Hum Mol Genet 27:2187–2204.

Brand AH, Perrimon N (1993) Targeted gene expression as a means of altering cell fates and generating dominant phenotypes. Development 118:401–415.

Brusich DJ, Spring AM, James TD, Yeates CJ, Helms TH, Frank CA (2018) *Drosophila* CaV2 channels harboring human migraine mutations cause synapse hyperexcitability that can be suppressed by inhibition of a Ca2+ store release pathway. PLoS Genet 14:e1007577.

Cárdenas C, Miller RA, Smith I, Bui T, Molgó J, Müller M, Vais H, Cheung K-H, Yang J, Parker I, Thompson CB, Birnbaum MJ, Hallows KR, Foskett JK (2010) Essential regulation of cell bioenergetics by constitutive InsP3 receptor Ca2+ transfer to mitochondria. Cell 142:270–283.

Chai A, Withers J, Koh YH, Parry K, Bao H, Zhang B, Budnik V, Pennetta G (2008) hVAPB, the causative gene of a heterogeneous group of motor neuron diseases in humans, is functionally interchangeable with its *Drosophila* homologue DVAP-33A at the neuromuscular junction. Hum Mol Genet 17:266–280.

Chaplot K, Pimpale L, Ramalingam B, Deivasigamani S, Kamat SS, Ratnaparkhi GS (2019) SOD1 activity threshold and TOR signalling modulate VAP(P58S) aggregation via reactive oxygen species-induced proteasomal degradation in a *Drosophila* model of amyotrophic lateral sclerosis. Dis Model Mech 12:dmm033803.

Chouhan AK, Ivannikov Mv, Lu Z, Sugimori M, Llinas RR, Macleod GT (2012) Cytosolic calcium coordinates mitochondrial energy metabolism with presynaptic activity. J Neurosci 32:1233–1243.

Coyne AN, Siddegowda BB, Estes PS, Johannesmeyer J, Kovalik T, Daniel SG, Pearson A, Bowser R, Zarnescu DC (2014) Futsch/MAP1B mRNA is a translational target of TDP-43 and is neuroprotective in a *Drosophila* model of amyotrophic lateral sclerosis. J Neurosci 34:15962–15974.

Daniels RW, Rossano AJ, Macleod GT, Ganetzky B (2014) Expression of multiple transgenes from a single construct using viral 2A peptides in *Drosophila*. PLoS One 9:e100637.

Deivasigamani S, Verma HK, Ueda R, Ratnaparkhi A, Ratnaparkhi GS (2014) A genetic screen identifies Tor as an interactor of VAPB in a *Drosophila* model of amyotrophic lateral sclerosis. Biol Open 3:1127–1138.

De Vos KJ, Mórotz GM, Stoica R, Tudor EL, Lau KF, Ackerley S, Warley A, Shaw CE, Miller CCJ (2012) VAPB interacts with the mitochondrial protein PTPIP51 to regulate calcium homeostasis. Hum Mol Genet 21:1299–1311.

Dietzl G, Chen D, Schnorrer F, Su K-C, Barinova Y, Fellner M, Gasser B, Kinsey K, Oppel S, Scheiblauer S, Couto A, Marra V, Keleman K, Dickson BJ (2007) A genome-wide transgenic RNAi library for conditional gene inactivation in *Drosophila*. Nature 448:151–156.

Ding L, Yang X, Tian H, Liang J, Zhang F, Wang G, Wang Y, Ding M, Shui G, Huang X (2018) Seipin regulates lipid homeostasis by ensuring calcium-dependent mitochondrial metabolism. EMBO J 37:e97572.

Dong R, Saheki Y, Swarup S, Lucast L, Harper JW, De Camilli P (2016) Endosome-ER contacts control actin nucleation and retromer function through VAP-dependent regulation of PI4P. Cell 166:408–423.

Duchen MR (1992) Ca(2+)-dependent changes in the mitochondrial energetics in single dissociated mouse sensory neurons. Biochem J 283:41–50.

Dumollard R, Marangos P, Fitzharris G, Swann K, Duchen M, Carroll J (2004) Sperm-triggered [Ca2+] oscillations and Ca2+ homeostasis in the mouse egg have an absolute requirement for mitochondrial ATP production. Development 131:3057–3067.

Feeney CJ, Karunanithi S, Pearce J, Govind CK, Atwood HL (1998) Motor nerve terminals on abdominal muscles in larval flesh flies, *Sarcophaga bullata*: comparisons with *Drosophila*. J Comp Neurol 402:197–209.

Fergestad T, Bostwick B, Ganetzky B (2006) Metabolic disruption in *Drosophila* bang-sensitive seizure mutants. Genetics 173:1357–1364.

Frere S, Slutsky I (2018) Alzheimer's disease: from firing instability to homeostasis network collapse. Neuron 97:32–58.

Gögel S, Wakefield S, Tear G, Klämbt C, Gordon-Weeks PR (2006) The *Drosophila* microtubule associated protein Futsch is phosphorylated by Shaggy/Zeste-white 3 at an homologous GSK3β phosphorylation site in MAP1B. Mol Cell Neurosci 33:188–199.

Gomez-Suaga P, Paillusson S, Stoica R, Noble W, Hanger DP, Miller CCJ (2017) The ER-mitochondria tethering complex VAPB-PTPIP51 regulates autophagy. Curr Biol 27:371–385.

Homyk T, Sheppard DE (1977) Behavioral mutants of *Drosophila melanogaster*. I. Isolation and mapping of mutations which decrease flight ability. Genetics 87:95–104.

Hua R, Cheng D, Coyaud É, Freeman S, Di Pietro E, Wang Y, Vissa A, Yip CM, Fairn GD, Braverman N, Brumell JH, Trimble WS, Raught B, Kim PK (2017) VAPs and ACBD5 tether peroxisomes to the ER for peroxisome maintenance and lipid homeostasis. J Cell Biol 216:367–377.

Hummel T, Krukkert K, Roos J, Davis G, Klämbt C (2000) *Drosophila* Futsch/22C10 is a MAP1B-like protein required for dendritic and axonal development. Neuron 26:357–370.

Ivannikov MV, Macleod GT (2013) Mitochondrial free Ca2+ levels and their effects on energy metabolism in *Drosophila* motor nerve terminals. Biophysical J 104:2353–2361.

Joiner MIA, Griffith LC (1997) CaM kinase II and visual input modulate memory formation in the neuronal circuit controlling courtship conditioning. J Neurosci 17:9384–9391.

Kamemura K, Chen C-A, Okumura M, Miura M, Chihara T (2021) Amyotrophic lateral sclerosis-associated Vap33 is required for maintaining neuronal dendrite morphology and organelle distribution in *Drosophila*. Genes Cells 26:230–239.

Kanekura K, Nishimoto I, Aiso S, Matsuoka M (2006) Characterization of amyotrophic lateral sclerosis-linked P56S mutation of vesicle-associated membrane protein-associated protein B (VAPB/ALS8). J Biol Chem 281:30223–30233.

Kashima R, Redmond PL, Ghatpande P, Roy S, Kornberg TB, Hanke T, Knapp S, Lagna G, Hata A (2017) Hyperactive locomotion in a *Drosophila* model is a functional readout for the synaptic abnormalities underlying fragile X syndrome. Sci Signal 10:eaai8133.

Kun-Rodrigues C, Ganos C, Guerreiro R, Schneider SA, Schulte C, Lesage S, Darwent L, Holmans P, Singleton A, Bhatia K, Bras J, Bras J; International Parkinson's Disease Genomics Consortium (IPDGC) (2015) A systematic screening to identify de novo mutations causing sporadic early-onset Parkinson's disease. Hum Mol Genet 24:6711–6720.

Landers JE, Leclerc AL, Shi L, Virkud A, Cho T, Maxwell MM, Henry AF, Polak M, Glass JD, Kwiatkowski TJ, Al-Chalabi A, Shaw CE, Leigh PN, Rodriguez-Leyza I, McKenna-Yasek D, Sapp PC, Brown RH (2008) New VAPB deletion variant and exclusion of VAPB mutations in familial ALS. Neurology 70:1179–1185.

Le Masson G, Przedborski S, Abbott LF (2014) A computational model of motor neuron degeneration. Neuron 83:975–988.

Lin G, Mao D, Bellen HJ (2017) Amyotrophic lateral sclerosis pathogenesis converges on defects in protein homeostasis associated with TDP-43 mislocalization and proteasome-mediated degradation overload. Curr Top Dev Biol 121:111–171.

Ling SC, Polymenidou M, Cleveland DW (2013) Converging mechanisms in ALS and FTD: disrupted RNA and protein homeostasis. Neuron 79:416–438.

Lytton J, Westlin M, Hanley MR (1991) Thapsigargin inhibits the sarcoplasmic or endoplasmic reticulum Ca-ATPase family of calcium pumps. J Biol Chem 266:17067–17071.

Mahr A, Aberle H (2006) The expression pattern of the *Drosophila* vesicular glutamate transporter: a marker protein for motoneurons and glutamatergic centers in the brain. Gene Expr Patterns 6:299–309.

Mao D, Lin G, Tepe B, Zuo Z, Tan KL, Senturk M, Zhang S, Arenkiel BR, Sardiello M, Bellen HJ (2019) VAMP associated proteins are required for autophagic and lysosomal degradation by promoting a PtdIns4P-mediated endosomal pathway. Autophagy 15:1214–1233.

Marques VD, Barreira AA, Davis MB, Abou-Sleiman PM, Silva WA, Zago MA, Sobreira C, Fazan V, Marques W (2006) Expanding the phenotypes of the Pro56SerVAPB mutation: proximal SMA with dysautonomia. Muscle Nerve 34:731–739.

McCormack JG, Denton RM (1993) The role of intramitochondrial Ca^{2+} in the regulation of oxidative phosphorylation in mammalian tissues. Biochem Soc Trans 21:793–799.

McVicker DP, Millette MM, Dent EW (2015) Signaling to the microtubule cytoskeleton: an unconventional role for CaMKII. Devel Neurobio 75:423–434.

Mitne-Neto M, Machado-Costa M, Marchetto MCN, Bengtson MH, Joazeiro CA, Tsuda H, Bellen HJ, Silva HCA, Oliveira ASB, Lazar M, Muotri AR, Zatz M (2011) Downregulation of VAPB expression in motor neurons derived from induced pluripotent stem cells of ALS8 patients. Hum Mol Genet 20:3642–3652.

Moustaqim-Barrette A, Lin YQ, Pradhan S, Neely GG, Bellen HJ, Tsuda H (2014) The amyotrophic lateral sclerosis 8 protein, VAP, is required for ER protein quality control. Hum Mol Genet 23:1975–1989.

Nishimura AL, Mitne-Neto M, Silva HCA, Richieri-Costa A, Middleton S, Cascio D, Kok F, Oliveira JRM, Gillingwater T, Webb J, Skehel P, Zatz M (2004) A mutation in the vesicle-trafficking protein VAPB causes late-onset spinal muscular atrophy and amyotrophic lateral sclerosis. Am J Hum Genet 75:822–831.

Nishimura AL, Al-Chalabi A, Zatz M (2005) A common founder for amyotrophic lateral sclerosis type 8 (ALS8) in the Brazilian population. Hum Genet 118:499–500.

Oka M, Fujisaki N, Maruko-Otake A, Ohtake Y, Shimizu S, Saito T, Hisanaga SI, Iijima KM, Ando K (2017) Ca2+/calmodulin-dependent protein kinase II promotes neurodegeneration caused by tau phosphorylated at Ser262/356 in a transgenic *Drosophila* model of tauopathy. J Biochem 162:335–342.

Paillusson S, Gomez-Suaga P, Stoica R, Little D, Gissen P, Devine MJ, Noble W, Hanger DP, Miller CCJ (2017) α-Synuclein binds to the ER–mitochondria tethering protein VAPB to disrupt Ca2+ homeostasis and mitochondrial ATP production. Acta Neuropathol 134:129–149.

Parkes TL, Elia AJ, Dickinson D, Hilliker AJ, Phillips JP, Boulianne GL (1998) Extension of *Drosophila* lifespan by overexpression of human SOD1 in motorneurons. Nat Genet 19:171–174.

Pennetta G, Hiesinger PR, Fabian-Fine R, Meinertzhagen IA, Bellen HJ (2002) *Drosophila* VAP-33A directs bouton formation at neuromuscular junctions in a dosage-dependent manner. Neuron 35:291–306.

Peretti D, Dahan N, Shimoni E, Hirschberg K, Lev S (2008) Coordinated lipid transfer between the endoplasmic reticulum and the Golgi complex requires the VAP proteins and is essential for Golgi-mediated transport. Mol Biol Cell 19:3871–3884.

Rangaraju V, Calloway N, Ryan TA (2014) Activity-driven local ATP synthesis is required for synaptic function. Cell 156:825–835.

Ratnaparkhi A, Lawless GM, Schweizer FE, Golshani P, Jackson GR (2008) A *Drosophila* model of ALS: human ALS-associated mutation in VAP33A suggests a dominant negative mechanism. PLoS One 3:e2334.

Roos J, Hummel T, Ng N, Klämbt C, Davis GW (2000) *Drosophila* Futsch regulates synaptic microtubule organization and is necessary for synaptic growth. Neuron 26:371–382.

Rossano AJ, Chouhan AK, Macleod GT (2013) Genetically encoded pH-indicators reveal activity-dependent cytosolic acidification of *Drosophila* motor nerve termini in vivo. J Physiol 591:1691–1706.

Roulin PS, Lötzerich M, Torta F, Tanner LB, van Kuppeveld FJM, Wenk MR, Greber UF (2014) Rhinovirus uses a phosphatidylinositol 4-phosphate/cholesterol counter-current for the formation of replication compartments at the ER-Golgi interface. Cell Host Microbe 16:677–690.

Sanhueza M, Zechini L, Gillespie T, Pennetta G (2014) Gain-of-function mutations in the ALS8 causative gene VAPB have detrimental effects on neurons and muscles. Biol Open 3:59–71.

Selfridge JE, E L, Lu J, Swerdlow RH (2013) Role of mitochondrial homeostasis and dynamics in Alzheimer's disease. Neurobiol Dis 51:3–12.

Şentürk M, Mao D, Bellen HJ (2019) Loss of proteins associated with amyotrophic lateral sclerosis affects lysosomal acidification via different routes. Autophagy 15:1467–1469.

Smith EF, Shaw PJ, De Vos KJ (2017) The role of mitochondria in amyotrophic lateral sclerosis. Neurosci Lett 710:132933.

Stoica R, Paillusson S, Gomez-Suaga P, Mitchell JC, Lau DH, Gray EH, Sancho RM, Vizcay-Barrena G, De Vos KJ, Shaw CE, Hanger DP, Noble W, Miller CC (2016) ALS/FTD-associated FUS activates GSK-3β to disrupt the VAPB–PTPIP51 interaction and ER–mitochondria associations. EMBO Rep 17:1326–1342.

Sullivan KMC, Scott K, Zuker CS, Rubin GM (2000) The ryanodine receptor is essential for larval development in *Drosophila melanogaster*. Proc Natl Acad Sci U S A 97:5942–5947.

Tantama M, Martínez-François JR, Mongeon R, Yellen G (2013) Imaging energy status in live cells with a fluorescent biosensor of the intracellular ATP-to-ADP ratio. Nat Commun 4:2550.

Taylor JP, Brown RH, Cleveland DW (2016) Decoding ALS: from genes to mechanism. Nature 539:197–206.

Tsuda H, Han SM, Yang Y, Tong C, Lin YQ, Mohan K, Haueter C, Zoghbi A, Harati Y, Kwan J, Miller MA, Bellen HJ (2008) The amyotrophic lateral sclerosis 8 protein VAPB is cleaved, secreted, and acts as a ligand for Eph receptors. Cell 133:963–977.

Vagnoni A, Bullock SL (2016) A simple method for imaging axonal transport in aging neurons using the adult *Drosophila* wing. Nat Protoc 11:1711–1723.

Venkatesh K, Hasan G (1997) Disruption of the IP3 receptor gene of *Drosophila* affects larval metamorphosis and ecdysone release. Curr Biol 7:500–509.

Verstreken P, Ly CV, Venken KJT, Koh TW, Zhou Y, Bellen HJ (2005) Synaptic mitochondria are critical for mobilization of reserve pool vesicles at *Drosophila* neuromuscular junctions. Neuron 47:365–378.

Viquez NM, Li CR, Wairkar YP, DiAntonio A (2006) The B' protein phosphatase 2A regulatory subunit well-rounded regulates synaptic growth and cytoskeletal stability at the *Drosophila* neuromuscular junction. J Neurosci 26:9293–9303.

Wong CO, Chen K, Lin Y, Chao Y, Duraine L, Lu Z, Yoon W, Sullivan JM, Broadhead GT, Sumner CJ, Lloyd TE, Macleod GT, Bellen HJ, Venkatachalam K (2014) A TRPV channel in *Drosophila* motor neurons regulates presynaptic resting Ca^{2+}levels, synapse growth, and synaptic transmission. Neuron 84:764–777.

Wong CO, Palmieri M, Li J, Akhmedov D, Chao Y, Broadhead GT, Zhu MX, Berdeaux R, Collins CA, Sardiello M, Venkatachalam K (2015) Diminished MTORC1-dependent JNK activation underlies the neurodevelopmental defects associated with lysosomal dysfunction. Cell Rep 12:2009–2020.

Wong CO, Karagas NE, Jung J, Wang Q, Rousseau MA, Chao Y, Insolera R, Soppina P, Collins CA, Zhou Y, Hancock JF, Zhu MX, Venkatachalam K (2021) Regulation of longevity by depolarization-induced activation of PLC-β-IP3R signaling in neurons. Proc Natl Acad Sci USA 118: e2004253118.

Woolums BM, McCray BA, Sung H, Tabuchi M, Sullivan JM, Ruppell KT, Yang Y, Mamah C, Aisenberg WH, Saavedra-Rivera PC, Larin BS, Lau AR, Robinson DN, Xiang Y, Wu MN, Sumner CJ, Lloyd TE (2020) TRPV4 disrupts mitochondrial transport and causes axonal degeneration via a CaMKII-dependent elevation of intracellular Ca2. Nat Commun 11:2679.

Xu L, Wang X, Zhou J, Qiu Y, Shang W, Liu J-P, Wang L, Tong C (2020) Miga-mediated endoplasmic reticulum-mitochondria contact sites regulate neuronal homeostasis. Elife 9:e56584.

Zhao YG, Liu N, Miao G, Chen Y, Zhao H, Zhang H (2018) The ER contact proteins VAPA/B interact with multiple autophagy proteins to modulate autophagosome biogenesis. Curr Biol 28:1234–1245.e4.